1 **Phenotypic pleiotropy of missense variants in human B cell-confinement receptor P2RY8**

2 Taylor N. LaFlam[1,2,3†*], Christian B. Billesbølle[4†], Tuan Dinh[5], Finn D. Wolfreys[2,6§], Erick Lu[2,6¶],

3 Tomas Matteson[,7,8‡], Jinping An[2,6], Ying Xu[2,6], Arushi Singhal[3], Nadav Brandes[9], Vasilis

4 Ntranos[5,8,10,11,12], Aashish Manglik[4,13,14,15], Jason G. Cyster[2,6*], Chun Jimmie Ye[3,5,7,8,10,11,13,16,17*]

5 Affiliations:

6 1: Division of Pediatric Rheumatology, Department of Pediatrics, University of California, San
7 Francisco, San Francisco, CA, USA

8 2: Department of Microbiology and Immunology, University of California, San Francisco, San
9 Francisco, CA, USA

10 3: Gladstone-UCSF Institute of Genomic Immunology, San Francisco, CA, USA

11 4: Department of Pharmaceutical Chemistry, University of California, San Francisco, San
12 Francisco, CA, USA

13 5: Department of Epidemiology and Biostatistics, University of California, San Francisco, San
14 Francisco, CA, USA

15 6: Howard Hughes Medical Institute, University of California, San Francisco, San Francisco,
16 CA, USA

17 7: Division of Rheumatology, Department of Medicine, University of California, San Francisco,
18 San Francisco, CA, USA

19 8: Institute for Human Genetics, University of California, San Francisco, San Francisco, CA,
20 USA

21 9: Department of Biochemistry and Molecular Pharmacology, New York University, New York,
22 NY, USA

23 10: Department of Bioengineering and Therapeutic Sciences, University of California, San
24 Francisco, San Francisco, CA, USA

25 11: Bakar Computational Health Sciences Institute, University of California, San Francisco, San
26 Francisco, CA, USA

27 12: Diabetes Center, University of California, San Francisco, CA, USA

28 13: Chan Zuckerberg Biohub, San Francisco, CA, USA

29 14: Quantitative Biosciences Institute, San Francisco, CA, USA

30 15: Department of Anesthesia and Perioperative Care, University of California, San Francisco,
31 San Francisco, CA, USA

32 16: Parker Institute for Cancer Immunotherapy, University of California, San Francisco, San
33 Francisco, CA, USA

34   17: Arc Institute, Palo Alto, CA, USA

35   §: Current affiliation: Department of Ophthalmology, University of California, San Francisco,
36   CA, USA

37   ¶: Current affiliation: Gilead Sciences, Foster City, CA, USA

38   ‡: Current affiliation: Retro Biosciences, San Francisco, CA, USA

39   †: These authors contributed equally to this work

40   *: Correspondence: taylor.laflam@ucsf.edu; jason.cyster@ucsf.edu; jimmie.ye@ucsf.edu.

41   **Abstract**

42   Missense variants can have pleiotropic effects on protein function and predicting these effects
43   can be difficult. We performed near-saturation deep mutational scanning of P2RY8, a G-protein-
44   coupled receptor that promotes germinal center B cell confinement. We assayed the effect of
45   each variant on surface expression, migration, and proliferation. We delineated variants that
46   affected both expression and function, affected function independently of expression, and
47   discrepantly affected migration and proliferation. We also used cryo-electron microscopy to
48   determine the structure of activated, ligand-bound P2RY8, providing structural insights into the
49   effects of variants on ligand binding and signal transmission. We applied the deep mutational
50   scanning results to both improve computational variant effect predictions and to characterize the
51   phenotype of germline variants and lymphoma-associated variants. Together, our results
52   demonstrate the power of integrating deep mutational scanning, structure determination, and in
53   silico prediction to advance the understanding of a receptor important in human health.

54

55   Missense variants, in which the amino acid sequence of a protein is altered, represent a crucial
56   class of genetic variation that can significantly impact protein function. Germline missense
57   variants are frequent in the human population[1,2], highly enriched for those causal for rare
58   Mendelian disorders, and statistically associated with common complex diseases[3]. Somatic
59   missense mutations are frequent in cancers and those of driver genes are a major contributor to
60   tumorigenesis[4,5]. Determining the effects of missense variants on protein function is essential for
61   diagnosing and understanding the genetic causes of human diseases[2,6].

62   Current approaches to missense variant annotation rely on both computational and experimental
63   methods. Emerging computational variant effect prediction (VEP) approaches using deep
64   learning can predict the effects of all missense mutations and have demonstrated success in
65   identifying variants that cause Mendelian diseases, most of which are loss-of-function (LoF)[6–8].
66   However, these algorithms are much less effective at identifying cancer driver mutations, which
67   are frequently gain-of-function (GoF) and not conserved evolutionarily[9,10]. Moreover, these tools
68   provide only a single functional prediction per variant, limiting their capacity to predict effects
69   across diverse phenotypes.

70 In parallel, the convergence of next-generation sequencing and massively-parallel gene synthesis
71 have propelled experimental profiling of large numbers of missense variants via deep mutational
72 scanning (DMS), also known as multiplexed assays of variant effect (MAVE)[11–13]. Unlike
73 computational predictions, DMS experiments can assess variant effects across multiple
74 phenotypes and cell types, offering rich, direct data on functional consequences. Furthermore,
75 because DMS does not depend on evolutionary conservation, they provide an unbiased approach
76 to variant characterization. DMS approaches remain low-throughput, and most human genes
77 have yet to be profiled. Nevertheless, the growing body of DMS data, including an international
78 collaborative effort to collate these results[14], represents a valuable resource that could ultimately
79 inform and refine computational VEP tools.

80 One application of these approaches is studying G-protein-coupled receptors (GPCRs), a large
81 family of ~800 transmembrane receptors that play important roles across numerous physiologic
82 pathways and are the most frequent drug targets in medicine[15,16]. Sensitivity to missense variants
83 generally varies between domains within a GPCR, as illustrated by the uneven distribution of
84 GPCR variants that cause Mendelian disorders[17]. Transducers of GPCR signaling include the
85 heterotrimeric G proteins, of which there are four major families, G_s, $G_{i/o}$, $G_{q/11}$, and $G_{12/13}$, as
86 well as the β-arrestins[18,19]. Several GPCRs have been the focus of DMS, revealing insights into
87 how missense variants affect their surface expression[20–22] and signaling[23,24]. Examining both
88 expression and function has the benefit of allowing one to distinguish between effects mediated
89 through, or independent of, changes in expression[24]. Despite this progress, GPCRs that signal
90 primarily through $G_{12/13}$ remain underexplored among DMS and structural studies[25].

91 P2RY8 is a G_{13}-coupled GPCR that is expressed on several lymphocyte subsets, including
92 germinal center (GC) B cells, where it restrains cell migration and proliferation[26–28]. Its ligand is
93 S-geranylgeranyl-L-glutathione (GGG)[29]. Addition of GGG in migration assays of P2RY8-
94 expressing cells causes activation of RhoA and inhibition of migration towards chemokines[30].
95 The *P2RY8* locus is located on the pseudoautosomal region of the X and Y chromosomes and is
96 frequently mutated in diffuse large B cell lymphoma (DLBCL) and Burkitt lymphoma[26,31,32]. In
97 addition, variants in P2RY8 have been identified in a small number of patients with lupus, and
98 these variants were found to affect B cell negative selection and plasma cell development when
99 expressed in mice[33].

100 The immunologic importance of P2RY8 and its restricted expression make it an attractive target
101 for therapeutic intervention, but the current understanding of how specific missense variants
102 affect its function is limited. To address this, we conducted DMS of P2RY8, evaluating surface
103 expression and two distinct functional outcomes, inhibition of migration and restraint of
104 proliferation. Using cryo-electron microscopy (cryo-EM), we determined the structure of P2RY8
105 in complex with its ligand, GGG, providing a structural scaffold for interpreting how missense
106 variants influence its active conformation and signaling. We also illustrate how integrating
107 relatively sparse experimental data from these screens can enhance the performance of
108 computational VEP tools. We performed in-depth validation of select variants, which provided
109 further insights into P2RY8 function, including evidence that receptor initiation of pathways
110 regulating migration and proliferation is at least partly distinct. In sum, we demonstrate the

111 utility of performing DMS on multiple functional phenotypes and the complementary benefits of
112 a multimodal approach to annotate the pleiotropic effects of missense variants of a GPCR to
113 better understand its biology.

Results

Deep mutational scanning of P2RY8 across three phenotypes

116 We performed deep mutational scanning of P2RY8, using a pooled lentiviral library of 7,045
117 variants covering all possible substitutions for 353/358 non-start codons and synonymous
118 variants for 338 positions (Supplemental Table 1). We transduced OCI-Ly8 (Ly8) cells, a human
119 DLBCL cell line, in which we previously knocked out endogenous P2RY8[29], and performed
120 three parallel screens: (1) receptor surface expression, (2) migration of cells simultaneously
121 exposed to chemoattractant CXCL12 and P2RY8 ligand GGG, and (3) proliferation across
122 multiple time points over 10 days (Fig. 1a and Extended Data Fig. 1a,b). Each of these three
123 screens were highly reproducible across four replicates, with pairwise Pearson correlation
124 coefficients (r) ranging from 0.96 to 0.97 for surface expression, 0.71 to 0.85 for migration, and
125 0.33 to 0.66 for proliferation (Extended Data Fig. 1c-e). Missense variants showed a bimodal
126 distribution of effect sizes (i.e., z-scores based on synonymous variant effects) across all three
127 assays (Fig. 1b,c and Extended Data Fig. 2a,b and Supplemental Table 2). Approximately half of
128 missense variants reduced the expression of surface P2RY8 but 365 variants increased
129 expression (Fig. 1c), suggesting GoF effects are detectable in our screens. As expected, the effect
130 sizes of variants on expression of P2RY8 are inversely correlated with their effects on migration
131 (Fig. 1c; Spearman correlation coefficient (ρ) of -0.837) and proliferation (Extended Data Fig.
132 2a, ρ = -0.614). The migration and proliferation effect sizes were also significantly correlated
133 (Extended Data Fig. 2b, ρ = 0.725).

134 Averaging the effect sizes across substitutions for each position resulted in higher inverse
135 correlation between migration and expression while also identifying several positions in which
136 missense variants consistently affected function but not expression (Fig. 1d and Extended Data
137 Fig. 2c,d). Mutation tolerance at specific positions varied significantly within each protein
138 domain; highly sensitive positions were enriched in the transmembrane helices (TM) and
139 extracellular loops (EC), whereas no position in the C-terminal domain (CTD) was highly
140 sensitive (Fig. 1e). Similar differences between domains were also observed when examining
141 the effect of individual variants, though large effect substitutions do exist in all domains
142 (Extended Data Fig. 2e). The range of variant effects within positions varied widely, with some
143 positions having similar effects for all missense variants and others having a large spread of
144 effects (Extended Data Fig. 2f,g).

Improving computational variant effect prediction using limited experimental data

146 ESM1b is a self-supervised protein language model that has been shown recently to have high
147 zero-shot predictive power of pathogenicity of coding variants[6]. We found that our DMS
148 expression effect sizes correlated well overall with the variant ESM1b scores (Fig 2a, ρ = 0.586).
149 However, there was a subset of variants in which decreased expression was not successfully
150 predicted (Fig. 2a). There was similar correlation between ESM1b scores and and migration

151   effect sizes but lower correlation with proliferation effect sizes (Fig. 2b,c; ρ = -0.593 for
152   migration and ρ = -0.500 for proliferation). When averaged by position the mean effect sizes
153   from the DMS were better correlated with mean ESM1b scores for all three assays (Fig. 2d-f).
154   Correlation between ESM1b and the DMS results varied by protein domain, with consistently
155   poor correlation within the CTD (Fig. 2g). Consistent with previous reports, we found that
156   ESM1b pathogenicity scores did not reliably distinguish between WT-like and GoF variants (Fig.
157   2h).

158   We investigated whether fine-tuning ESM1b with limited amounts of training data from our
159   DMS screen would yield a better supervised predictor of DMS results. Across training sets of 2,
160   3, 5, 7, 9, and 11 variants per position, we observed a sharply increased correlation between
161   predicted scores and the DMS effect sizes with just 2 variants per position, with further
162   improvements with increasing variants per position (Fig. 2i). For example, for the expression
163   data, correlation was ρ = 0.586 with base ESM1b scores but the mean ρ was 0.736 after training
164   with 2 variants per position (~10% of the DMS data), 0.794 with 5 variants per position, and
165   0.829 with 11 variants per position. Across all three phenotypes, 2 variants per position produced
166   ~60% as much improvement as was achieved with 11 variants per position. The fine-tuning
167   included a final ridge regression step as we observed that this resulted in greater increases in
168   correlation, particularly with smaller training sets (Extended Data Fig. 3a).

169   Given the significant overall gains observed even with 2 variants per position, we then examined
170   the degree to which domain-specific changes were observed. We observed the most striking
171   improvement within the NTD and the smallest amount of improvement within the CTD, with
172   intermediate improvements for other domains (Fig. 2j). Training with 11 variants per position
173   showed further improvements though correlation in the CTD remained modest (Fig. 2j). The
174   influence of the base ESM1b remained evident, with domains with higher correlations with base
175   ESM1b continuing to be the domains with higher correlations after fine-tuning, with the
176   exception of the NTD, for which base ESM1b was poorly predictive but even modest amounts of
177   training data resulted in a large improvement.

178   The improved correlation was visible when plotting fine-tuned ESM1b and DMS expression
179   effect sizes relative to plotting with baseline ESM1b (Extended Data Fig. 3b, relative to Fig. 2a).
180   Compared with what was seen with base ESM1b, there was marginally better separation between
181   the WT-like and GoF variants with 2 variants per position training, with improved separation
182   with 11 variants per position, though some overlap remained (Fig. 2k). These findings suggest
183   that although a screen with as few as two variants per position can enhance predictions of variant
184   effects, identification of GoF variants will likely require more intensive experimental analysis,
185   barring the development of new, superior VEP algorithms.

186   To ensure these observations were not unique to ESM1b, we also compared our DMS results
187   with an alternative VEP tool, AlphaMissense (AM). AM was produced through fine tuning
188   AlphaFold on human and primate population variant frequencies and has been shown to have
189   state-of-the-art zero-shot performance at predicting DMS results[7,34]. We observed high
190   correlation between AM scores and the expression, migration, and proliferation effect sizes, in
191   fact with higher correlation in each case than for ESM1b (Extended Data Fig. 4a-c). Similarly,

192 correlation was again higher for the position-averaged data compared to individual variant data
193 (Extended Data Fig. 4d-f). As with ESM1b, correlation between AM and the DMS data varied
194 by protein domain, with much lower correlation with the CTD (Extended Data Fig. 4g). As with
195 ESM1b, AM better distinguished between LoF variants and WT-like variants than between GoF
196 variants and WT-like variants (Extended Data Fig. 4h). LoF variants that had a benign AM
197 pathogenicity score[7] were overrepresented in the EC, IC, and CTD domains relative to correctly
198 assigned LoF variants (Extended Data Fig. 4i). In addition, these misclassified variants were
199 overrepresented at positions in which the WT amino acid is positively charged and among
200 variants in which the substituted amino acid was glycine or an aliphatic hydrophobic residue
201 (Extended Data Fig. 4i).

202 Fine-tuning comparable to what was performed with ESM1b was not possible with AM given the
203 specific model weights are not publicly available. However, concurrently with the ESM1b fine-
204 tuning described above, we also implemented the augmented one-hot encoded (OHE) ridge
205 regression model previously described[35], using the same variant training sets as in the fine-tuning
206 iterations. This resulted in improved correlation between predicted scores and the DMS effect
207 sizes, with greater gains with increasing training set size (Extended Data Fig. 4k). The degree of
208 improvement was less than was seen with ESM1b fine-tuning, though given the higher baseline
209 correlation, the absolute correlations differences were smaller between the two (Extended Data
210 Fig. 3c). The improvements with OHE-regression with ESM1b were also less than those seen
211 from fine-tuning ESM1b, particularly with larger training sets (Extended Data Fig. 3d). In
212 summary, two different approaches using a subset of our DMS data were able to improve variant
213 effect prediction relative to two distinct state-of-the-art VEP tools alone.

214 Finally, we investigated whether the DMS results for P2RY8 could be used to improve variant
215 effect prediction for another GPCR. Recently a DMS study was published for GPR68, a pH
216 sensing receptor that like P2RY8 is a class A, subgroup δ GPCR[24]. The correlations between
217 ESM1b scores and GPR68 DMS scores for missense variants were $\rho = 0.560$ for surface
218 expression and $\rho = 0.529$ for pH 5.5 signaling, comparable to what was seen with P2RY8. We
219 found that after fine-tuning ESM1b on P2RY8 DMS expression with 300 optimization steps,
220 there was no improvement in variant effect prediction for GPR68 (Fig. 2l), with a Spearman
221 correlation difference of <0.005 for both GPR68 expression and function. We restricted to 50
222 optimization steps to reduce overfitting and now observed a small increase in correlation of
223 ~0.02, in comparison to ~0.13-0.15 increase within P2RY8 itself after training with 2 variants
224 and ~0.21-0.24 increase after training with 11 variants (Fig. 2j). We did observe varying effects
225 by protein domain, with the greatest improvement in the TM domain for expression and function,
226 with significant gains in ICL and H8 regions for expression as well (Fig. 2m). This finding
227 corresponds to greater conservation of these regions across GPCRs[36,37].

228 In summary, use of a subset of our DMS data was able to strongly improve variant effect
229 prediction relative to two distinct state-of-the-art VEP tools alone, but showed limited ability to
230 generalize to improvements in variant effect predictions in a different GPCR.

231 **Validation of variants with independent effects on expression and function**

232 Although there was overall inverse correlation between variant effects on cell migration and
233 surface expression, we identified several hundred variants that affected migration independent of
234 expression but not vice versa, consistent with the hierarchical nature of these phenotypes (Fig.
235 1c). We computed an expression-adjusted migration score, and identified 25 residues with
236 substantially higher mean effect size across substitutions in migration than in expression; 23/25
237 of these positions were located within a transmembrane helix or extracellular loop (Fig. 3a).
238 Plotting the expression-adjusted migration score by position across the protein sequence showed
239 several peaks, including in TM3 into ICL2, in ECL2, and in TM6 into ECL3 (Fig. 3b). The first
240 region includes the canonical D(E)-R-Y motif that is critical for GPCR signaling[18]. These 25
241 positions also generally had larger mean effect sizes on proliferation than expression (Extended
242 Data Fig. 5a). Performing a comparable analysis on migration and proliferation, there were only
243 six positions with a high migration-adjusted proliferation scores and none with the converse (Fig.
244 3c).

245 We performed validation studies of several variants, drawing from different regions of the
246 protein and representative of various migration and proliferation phenotypes with preserved
247 surface expression: increased migration and proliferation (F103^{3x32}L, G124^{3x53}E, W181^{ECL2}D,
248 L220^{5x65}Y), decreased migration and proliferation (A34^{1x43}F, S44^{1x53}C, G237^{6x35}N, A240^{6x38}T),
249 increased migration relative to proliferation (T68^{2x49}K, Y104^{3x33}I, K180^{ECL2}I), increased
250 proliferation relative to migration (V29^{1x38}W, W181^{ECL2}M, W181^{ECL2}S), and WT-like function
251 (T330^{CTD}N) (Fig. 3d). (Superscripts refer to generic GPCR residue numbering per revised
252 Ballesteros-Weinstein method for class A GPCRs[36,38].) These variants include four of the
253 positions with high expression-adjusted migration scores (Fig. 3a) and one of the residues with
254 high migration-adjusted proliferation scores (Fig. 3c). All variants were confirmed to support
255 surface expression, and high correlation was observed between screen and validation results for
256 these 15 variants (Fig. 3e,f; r = 0.506 with p-value = 0.0543). The inclusion of 8 additional
257 P2RY8 variants that we have previously characterized[26,29] resulted in a higher correlation (r =
258 0.799, p-value < 0.0001). Despite P2RY8 expression, cells with these variants showed a range of
259 migratory capacity toward CXCL12 in the presence of GGG (Fig. 3g). We observed high
260 correlation between the screen and validation at both high and low GGG exposure (100 nM, r =
261 0.493 with p-value = 0.1427, though Spearman ρ = 0.661 with p-value = 0.044; 10 nM, r =
262 0.728, p-value = 0.0031) (Fig. 3h). We also performed validation proliferation studies,
263 comparing change in relative abundance of transduced and untransduced cells over a 13-day
264 span. Over that time, WT P2RY8 results in ~2/3 reduction in frequency compared to
265 untransduced cells. Although the effects of the variants on proliferation appeared largely in
266 agreement with those seen in the screen, the trend was not statistically significant (Fig. 3i,j). In
267 summary, individual variant validation across all three assays yielded findings that were in close
268 accord with the screen.

269 **Structure of activated ligand-bound human P2RY8**

270 To facilitate understanding of the structural basis of the variant phenotypes revealed by the DMS,
271 we used cryo-EM to determine the structure of activated, GGG-bound human P2RY8. We
272 generated a C-terminal fusion of P2RY8 with a minimized and stabilized version of Gα$_{13}$

273 (miniG$_{13}$) as previously described for other heterotrimeric G proteins[39,40] (Extended Data Fig.

274 6a). P2RY8-miniG$_{13}$ was purified in the presence of GGG and further complexed with

275 recombinant Gβ1γ2 (Extended Data Fig. 6b). The resulting preparation was analyzed by single-

276 particle cryo-EM, which yielded a 2.7 Å map of the complex (Extended Data Fig. 7 and

277 Supplemental Table 3). While the receptor and miniG$_{13}$ are well resolved, only a portion of the

278 Gβ$_1$ was visible in the resulting density; the majority of Gγ$_2$ was not resolved. Importantly, the

279 map revealed a density consistent with GGG located in the canonical class A GPCR orthosteric

280 ligand-binding pocket (Fig. 4a,b).

281 We next mapped DMS functional results onto the receptor structure, which illustrated the

282 structural elements most essential for expression and migration inhibition (Fig. 4c,d). As

283 observed in scatter plots of the DMS data (Fig. 1d), there was substantial correlation between

284 P2RY8 residues required for expression and migration inhibition. Variants of positions that lead

285 to decreased P2RY8 expression are primarily concentrated in the TM regions, with EC and IC

286 loops more tolerant to variants. Similarly, most TM variants cause decreased migration

287 inhibition. To identify positions important for migration that do not simply affect protein

288 expression, we also mapped expression-adjusted migration scores (Fig. 4e). This analysis

289 revealed two critically important regions: residues surrounding the GGG ligand and key

290 interacting residues with Gα$_{13}$ (Fig. 4f).

291 The P2RY8 interaction with miniGα$_{13}$ is highly similar to the canonical conformation observed

292 for most GPCR-G protein complexes to date[37,41]. Our DMS provides an unbiased view of key

293 regions of P2RY8 that are important for signal transduction. We observed that six residues

294 directly contacting miniGα$_{13}$ had high expression-adjusted migration scores: R121^{3x50}, G124^{3x53},

295 V125^{3x54}, L129^{34x51}, Y213^{5x58}, and A235^{6x33} (Fig. 3a and 4f), and two reisdues had high

296 migration-adjusted proliferation scores: M52^{ICL1} and S56^{2x37}. Although we lack an inactive state

297 structure of P2RY8, the importance of these residues is underscored by their conservation among

298 class A GPCRs and key contacts they make to stabilize P2RY8 or interact with Gα$_{13}$. For

299 example, both R121^{3x50} and Y213^{5x58} directly bind to the α5 helix of miniGα$_{13}$ (Fig. 4g). As has

300 been observed previously for many class A GPCRs, Y213^{5x58} engages Y293^{7x53} in a bonding

301 network that likely stabilizes active P2RY8. Additionally, L129^{34x51} binds to a conserved

302 hydrophobic cavity in Gα$_{13}$ (Fig. 4h). Plotting the average DMS effect sizes for all 38 P2RY8

303 positions in contact with miniGα$_{13}$ showed a range of mutation tolerance ranging from highly

304 sensitive for both expression and migration to largely tolerant (Fig. 4i). Individual missense

305 variants for two of these positions, G124^{3x53}E and L220^{5x65}Y, were including in the variant

306 validation set already described; both of these variants were expressed but strongly deleterious to

307 function (Fig. 3e,g,i). Taken together, the DMS results and cryo-EM structure provide

308 complementary, concordant insights into receptor function.

Structural features of GGG recognition

310 GGG binds to P2RY8 in a large solvent-facing cavity, with a combination of hydrophilic

311 interactions with the glutathione headgroup and hydrophobic interactions along the

312 geranylgeranyl tail (Fig. 5a and Extended Data Fig. 8). The glutathione headgroup is located

313 towards the extracellular side of the pocket, while the geranylgeranyl tail extends deeply within

314 the core of the receptor. Of the 28 residues that contact GGG, ten of the residues are among those
315 with high expression-adjusted migration scores (Fig. 3a and 5b). Several of these high scoring
316 positions contact the GGG headgroup, including K180^{ECL2}, H260^{6x58}, R264^{ECL3}, and Y272^{7x32}.
317 Residues H260^{6x58}, R264^{ECL3}, and Y272^{7x32} engage the glutamate residue in GGG, with H260^{6x58}
318 making a direct hydrogen bond with the carboxylic acid. Additionally, several positions contact
319 the proximal geranylgeranyl tail closest to the thioether cysteine in GGG; these include L179^{ECL2},
320 W190^{5x35}, L194^{5x39}, and L265^{ECL3}. In addition, two residues in contact with the GGG headgroup,
321 G8^{NTD} and W181^{ECL2}, have high migration-adjusted proliferation scores (Fig. 3c). Validation
322 assays described above included examined variants in three residues in the GGG-binding pocket,
323 Y104^{3x33}I, K180^{ECL2}I, and W181^{ECL2}M, all of which showed decreased proliferation restraint and
324 two of which showed decreased migration inhibition (Fig. 3g,i). Examination of the DMS results
325 for all binding pocket residues showed significant intolerance to mutation for most positions
326 (Fig. 5c). Positions with high expression-adjusted migration scores were significantly enriched
327 among both the GGG-binding pocket positions and the Gα_{13}-contacting positions (Fig. 5d).
328 Similarly, 17/25 residues with high expression-adjusted migration scores were either part of the
329 GGG-binding pocket or in contact with Gα_{13}, a significant enrichment from 49/286 among non-
330 CTD residues without high expression-ajusted migration scores (p < 0.0001, Fisher's exact test).

331 Residues surrounding the deeper portion of the GGG-binding pocket were more tolerant to
332 mutation (Fig. 5b). Our DMS results therefore suggest that the glutathione headgroup combined
333 with the proximal prenyl group in the geranylgeranyl tail are required for P2RY8 activation. We
334 tested our DMS-driven model for the most important chemical components of GGG required for
335 P2RY8 activation with analogs. We previously showed that glutathione alone and
336 geranylgeranyl-pyrophosphate are both inactive at P2RY8[29]. As we demonstrated previously the
337 cysteinyl leukotriene C$_4$ (LTC$_4$) is active at P2RY8 with ~100-fold less potency in a migration
338 inhibition assay than GGG[29]. Although the specific orientation of LTC$_4$ within the P2RY8
339 binding site is uncertain, it is likely that the glutathione headgroup and the aliphatic tail of LTC$_4$
340 occupy similar general positions as GGG. The ability of LTC$_4$ to activate P2RY8 suggested that
341 the specific shape of the geranylgeranyl tail of GGG is not required for P2RY8 activation.
342 Indeed, a saturated 16-carbon chain and a 15-carbon farnesyl group, which is one prenyl group
343 smaller than geranylgeranyl, both activated P2RY8 with ~10-fold less potency than GGG (Fig.
344 5e). Further diminutions in tail size significantly reduced potency, as seen for glutathione
345 conjugated to a single prenyl group (~1000-fold less potent than GGG) and glutathione
346 conjugated to a saturated 8-carbon chain (~5000-fold less potent than GGG). In sum, these
347 results illustrated ligand potency varied with the degree of contact possible between the
348 hydrophobic tail and P2RY8 within the binding site. The degree to which alterations in the
349 glutathione head affect activity and potency remain an area for future research.

Significant functional phenotypes with subtle proximal signaling changes

351 The specific points at which the P2RY8 signaling pathways affecting migration and proliferation
352 diverge have not been established, but our screen results suggested that biased agonism of these
353 activities was possible; on initial validation, V29^{1x38}W (V29W) and W181^{ECL2}M (W181M)
354 showed WT-like behavior in migration but decreased proliferation restraint, whereas K180^{ECL2}I

355   (K180I) showed decreased but not absent function in both phenotypes (Fig. 3g,i). K180I and
356   W181M are part of the GGG-binding pocket (Fig. 5a) whereas V29W is in TM1. We performed
357   more in-depth validation of these variants to explore the mechanism for these phenotypes.

358   We first examined migration inhibition across a range of GGG concentrations, with results
359   consistent with those from initial validation: W181M inhibited more strongly than WT at low
360   GGG concentrations (3 nM) and comparably to WT at higher GGG concentrations; V29W was
361   WT-like at all concentrations; K180I inhibited migration less than WT at all but very high GGG
362   concentrations (Fig. 6a). A different pattern was observed when examining proliferation with a
363   range of exogenous GGG concentrations. (We had not added exogenous GGG to the culture in
364   the proliferation arm of the screen or initial validation because we had previously observed that
365   B cells and B cell lines secrete GGG in amounts sufficient to affect proliferation[28,29,33].) In this
366   case, it was W181M that was most different from WT at lower GGG concentrations but
367   equivalent at high concentrations; V29W had a similar but less striking pattern; K180I had a
368   moderate deficit at all GGG concentrations relative to WT (Fig. 6b). In sum, although all three
369   variants were able to restrain proliferation and migration when exposed to high levels of GGG, at
370   low levels W181M showed greater defects in proliferation restraint and K180I greater defects in
371   migration inhibition (Fig. 6a-c). This provided evidence that the P2RY8 signaling that drives
372   these two processes is different at the receptor itself.

373   We then assayed elements of the known P2RY8 signaling pathway. It has previously been shown
374   that P2RY8 activation results in decreased phosphorylation of Akt and Erk and that deleterious
375   P2RY8 variants can disrupt this effect[29,33]. We used phospho-flow to assess simultaneously the
376   phosphorylation status of these two kinases for the three variants of interest. As expected, WT
377   P2RY8 allowed 100 nM GGG to trigger a significant reduction in the frequency of pAkt$^+$ cells.
378   Similar reductions were seen for all three interrogated variants (Fig. 6d). For all variants, GGG
379   also drove a decrease in pErk$^+$ cells, but K180I did so less effectively than WT (Fig. 6e). Overall,
380   the phospho-flow results showed less separation between WT P2RY8 and the variants than was
381   seen in the migration and proliferation assays.

382   We then used two luciferase-based reporter assays to assess variant effects on signaling pathway
383   elements more proximal to the receptor. To examine trimeric G-protein activation, we used
384   TRUPATH, a BRET-based approach[42,43]. In this system, luciferase is fused to Gα_{13}; when it
385   encounters its substrate, it can trigger fluorescence of GFP fused to Gγ. Activation of the trimeric
386   G-protein results in dissociation of the complex and decreased GFP signal relative to luciferase
387   signal. L220^{5x65}Y, a residue that interacts with Gα_{13} and was deleterious in initial validation
388   studies (Fig. 3g,i), was unable to drive G-protein activation (Fig. 6f). In contrast, WT P2RY8,
389   V29W, K180I, and W181M were all able to do so in a dose-responsive manner with comparable
390   IC$_{50}$ values (Fig. 6f). Although the variants showed a larger absolute change than WT, the degree
391   to which this reflected differences in expression versus intrinsic per-receptor maximum activity
392   was not determined. To measure β-arrestin recruitment, we used the NanoBiT system[44]. In this
393   system, a large fragment of luciferase is fused to the GPCR and a small fragment to β-arrestin.
394   When the GPCR and β-arrestin are in close proximity, the two luciferase fragments interact to
395   form a functional luciferase. As expected, a GPCR (β2AR) with a different ligand from P2RY8

396   was unable to recruit β arrestin with the addition of GGG (Fig. 6g). In contrast, WT, V29W,
397   K180I, and W181M all showed robust recruitment, with W181M having higher maximum
398   recruitment, though not significantly different EC_{50} (Fig. 6g). L220[5x65]Y showed significantly
399   reduced recruitment but was distinguishable from β AR. In sum, neither of these assays provided
400   a mechanistic explanation for the differential effects of these variants on migration and
401   proliferation.

402   For many though not all GPCRs, β-arrestin recruitment promotes receptor internalization[19]. We
403   examined changes in receptor surface expression after 45 minutes of exposure to various
404   concentrations of GGG. V29W showed a similar pattern to WT, whereas W181M had a higher
405   baseline expression and less relative decrease at 100 nM, and K180I had a lower baseline
406   expression but only modest reduction in surface expression even at high GGG concentrations
407   (Fig. 6h). The results of the NanoBiT β-arrestin assay and this internalization assay together
408   suggest that the ability to recruit β-arrestin is not sufficient to produce a normal P2RY8
409   internalization response to ligand. In sum, although dose-response studies further validated the
410   migration and proliferation phenotypes, assays of proximal signaling elements did not delineate
411   the specific mechanism underlying these phenotypes.

Disparate migration and proliferation phenotypes of two P2RY8 variants in vivo

413   Given their contrasting phenotypes in vitro as described above (Fig. 6a-c), we decided to further
414   assay the function of K180I and W181M in vivo. P2RY8, although conserved across vertebrates,
415   has been lost in rodents. However, previous work has illustrated that human P2RY8 introduced
416   into mice is able to function to affect B cell positioning in lymphoid follicles and GC B cell
417   abundance in Peyer's patches[28,29]. To examine the effect of these mutants on B cell positioning in
418   lymphoid tissues, polyclonal murine B cells were activated in vitro, transduced with variant or
419   WT P2RY8, and then co-transferred into pre-immunized mice before harvest for
420   immunofluorescent microscopy analysis. The variant vectors contained GFP whereas the WT
421   vector contained TagBFP, permitting direct comparison within the same recipient mice. We have
422   previously shown that in the absence of P2RY8, transferred activated B cells do not localize into
423   the GC, whereas most cells with WT P2RY8 congregate within the GC[28]. We observed this same
424   localization pattern with WT P2RY8-transduced B cells, with approximately 80% of TagBFP[+]
425   cells within the follicle being located in the GC (Fig. 6i,j). For both K180I and W181M,
426   approximately half of the transduced cells within the follicle were in the GC (Fig. 6i,j). This in
427   vivo phenotype is consistent with the modest migration inhibition defect seen in in vitro for
428   K180I. The mechanism for the decreased localization of W181M in vivo compared to WT,
429   despite at least WT-like responsiveness in vitro, is less evident. Although previous direct GGG
430   measurement in lymphoid tissue homogenates found a concentration of approximately 10 nM[29],
431   the interstitial concentrations at different sites within the lymphoid tissue are uncertain aside
432   from a relatively lower level within the GC[28,29]. The in vivo behavior differences for W181M
433   compared to WT that contrast with the in vitro migration assay (Fig. 6a) may be a consequence
434   of other differences resulting from this variant, including higher baseline surface expression and
435   decreased internalization in response to ligand, differences in response kinetics, and more
436   complicated chemokine and GGG gradients in vivo compared to the transwell assay.

437 In a second in vivo assay, we used transduced bone marrow to reconstitute irradiated congenic
438 mice, and after reconstitution we compared the proportion of transduced cells among GC and
439 follicular B cells in three tissues. We have previously shown that WT P2RY8-transduced cells are
440 less prevalent among GC B cells than follicular B cells in Peyer's patches, whereas there is not a
441 significant difference in mesenteric lymph nodes or spleen[28]. The current experiments
442 reproduced this effect for WT; in contrast, neither K180I nor W181M showed altered prevalence
443 in GC compared to follicular B cells in any of the three tissues (Fig. 6k and Extended Data Fig.
444 9a,b). This argues that the phenotype produced by WT P2RY8 requires a high degree of receptor
445 activity, and that even moderate defects in proliferation restraint, as seen in vitro with K180I
446 (Fig. 5b), result in inability to recapitulate the WT in vivo growth-regulation phenotype. The still
447 greater deficit of W181M at physiologic ranges of GGG in vitro (Fig. 5b) would therefore also
448 translate to inability to recapitulate the phenotype produced by WT P2RY8. Overall, the results
449 of these in vivo assays provide the first evidence that it is possible for P2RY8-driven
450 confinement within the GC to occur without causing decreased prevalence within the GC B cell
451 pool.

Phenotypes of germline and lymphoma-associated P2RY8 variants

453 Hundreds of missense variants in P2RY8 have been observed in human population sequencing
454 studies, distributed across the protein and with highly varied phenotypes per our DMS results
455 (Fig. 7a). Most such variants are rare or very rare but comparison of allele frequency in the
456 gnomAD data set[2] with their DMS effect sizes nonetheless revealed statistically significant
457 correlations, consistent with selective pressure. These are apparent both when the 476 individual
458 variant frequencies are considered and when consolidating these variants within the 260 involved
459 positions (Fig. 7b and Extended Data Fig. 10a-e). Four of the variants validated above (Fig.
460 3e,g,i) are among the variants reported in gnomAD (F103^{3x32}L, which shows LoF, and
461 G237^{6x36}N, A240^{6x39}T, and T330^{CTD}N, which are WT-like).

462 P2RY8 missense variants are common in two GC B-cell-derived lymphomas, DLBCL and
463 Burkitt lymphoma. We plotted the effect sizes of 48 variants compiled from two sources
464 (COSMIC[32,45] and Muppidi et al.[26]) and observed that nearly all of these variants reduced P2RY8
465 expression and decreased its migration inhibition, and none of them showed increased expression
466 or function relative to WT (Fig. 7c). Although 15 of these variants have been observed in
467 gnomAD as germline variants, none have an allele frequency > 0.0001, indicating it is very
468 likely that they were somatically acquired in these cancers. Of the 41 positions with lymphoma
469 variants, six were identified above (Fig. 3a) as having high expression-adjusted migration scores
470 (F103^{3x32}, Y104^{3x33}, A191^{5x36}, A235^{6x34}, R264^{ECL3}, and F266^{ECL3}). In addition, another involved
471 position, Y30^{1x39}, has the highest mean proliferation effect size of any position (Fig. 3c). These
472 lymphoma variants involve residues found to interact with Gα$_{13}$, including M62^{2x43}, A235^{6x34},
473 and S297^{8x47}, and residues in the GGG-binding pocket, including Y104^{3x33}, F176^{ECL2}, D177^{ECL2}
474 and R264^{ECL3}. Of the three lymphoma variants with a large migration effect size but no decrease
475 in expression (Fig. 7c), two involve R264^{ECL3}: R264C and R264H. In addition, our screen
476 revealed that six of the lymphoma variants that are LoF would not have been classified as

477 pathogenic based on AM pathogenicity score (P20^{1x29}L, R86^{ECL1}C, A140^{4x42}T, R264^{ECL3}H,
478 S270^{ECL3}N, and K276^{7x36}R; Supplemental Tables 1 and 2).

479 Turning to 159 missense variants that have been identified in non-hematologic cancers
480 (COSMIC), we observed a broadly distributed set of phenotypes akin to that seen in germline
481 variants (Fig. 7d). Although 67 of these variants are present in gnomAD, only 3 have an
482 observed allele frequency > 0.0001 (V125^{3x54}I, R133^{34x55}P, V333^{CTD}L), again suggesting
483 predominantly somatic mutagenesis. Ten of these variants are also present in the DLBCL/Burkitt
484 lymphoma set. Comparison of the phenotype distributions for these four sets of variants using
485 Kolmogorov-Smirnov tests revealed statistically significant differences, with gnomAD and non-
486 hematologic cancer variants containing fewer deleterious variants than the set of all missense
487 variants, and DLBCL/Burkitt lymphoma variants being enriched for deleterious variants (Fig. 7e
488 and Extended Data Fig. 10f). These findings aligned with previous observations supporting
489 P2RY8 as a cancer driver gene in DLBCL and Burkitt lymphoma, in contrast to non-hematologic
490 cancers in which P2RY8 variants are more likely passenger mutations.

Discussion

492 Here, we report near-saturation DMS of human P2RY8, a G$_{13}$-coupled GPCR important for GC
493 B cell confinement, defining the expression, migration, and proliferation phenotypes for these
494 variants. Use of these different phenotypic readouts allowed for delineation of variants that
495 affected both expression and function, affected function independently of expression, and
496 discrepantly affected migration and proliferation.

497 VEP algorithms have improved significantly and, particularly at the position level, are highly
498 accurate at identifying changes that will result in loss of protein function. In P2RY8, however,
499 these methods are much less able to predict increases in protein expression or activity, echoing
500 similar limitations in VEP analysis of other proteins[7,9]. Our work demonstrates that it is possible
501 to generate new, more highly correlated prediction scores through the combination of VEP scores
502 and limited amounts of experimental data; even 2 variants per position resulted in a substantial
503 improvement. Although greater gains were achievable with actual fine-tuning of the protein
504 language model itself, even an OHE regression-based approach, which does not require
505 knowledge of the model weights, achieved significant improvements. Despite these sizeable
506 improvements in predictions for P2RY8 itself, use of P2RY8 experimental data could only
507 modestly improve variant effect predictions for a recently profiled GPCR, GPR68. It is possible
508 that alternative approaches to fine-tuning might enhance the ability to generalize from one
509 receptor to another. Our results suggest that predictions across a family of GPCRs can be
510 achieved more efficiently by profiling relatively few variants across many receptors, rather than
511 comprehensively profiling variants within a small number of receptors. Beyond single missense
512 variants, future studies could assay the combinatorial effects of multiple variants, indels, and
513 other structural variants, in order to enhance our understanding and ability to computationally
514 predict epistasis in GPCRs.

515 The structure of activated P2RY8 provides further understanding of the functional data obtained
516 through the DMS. By identifying key residues involved in interactions with Gα$_{13}$ and GGG, as

517 well as our work evaluating the potency of several alternative ligands, we lay the groundwork for
518 additional studies aimed at developing alternative agonist and antagonist ligands of this receptor.

519 Our exploratory studies of in-depth validation of select variants highlighted areas for continued
520 investigation. In particular, the mechanism by which a given variant may produce different
521 degrees of defects in migration or proliferation restraint remains unclear, particularly as the
522 assays of trimeric G-protein activity and β-arrestin recruitment did not show clear differences
523 that might explain these phenotypes. This highlights the ability of our phenotypic screens to
524 detect subtle phenotypes that may otherwise be missed in classical GPCR signaling assays that
525 report changes more proximal to the receptor. We believe that results from our screens provide a
526 more complete picture of how P2RY8 activation manifests as a phenotype, by intergrating the
527 compounding and amplified effects that resulting in subtle shifts in signal propagation through
528 the cell. Future study into the basis for these variants' phenotypes will be useful in further
529 defining P2RY8 function. Additionally, P2RY8 variants identified in this study will enable in
530 vivo studies to probe the role of P2RY8 function in GCs[29], B cell negative selection[33], and T cell
531 responses[28].

532 One caveat of our work is that the range of observed effect sizes is greater for expression than for
533 migration and both are greater than for proliferation. This may reflect details of the screen itself,
534 in which the maximum possible enrichment differs between the readouts. Adjustments, such as
535 running the proliferation assay for a longer period of time, could conceivably result in increased
536 effect sizes thereby enhancing phenotyping of proliferation.

537 Our work provides a resource for interpretation of the pathogenicity of nearly any given
538 missense variant of P2RY8, whether germline or somatic, which may be of particularly utility in
539 the setting of autoimmunity where deleterious P2RY8 variants have already been identified in a
540 small number of patients[33]. It also allows interpretation of any somatic P2RY8 variants observed
541 in cancer, including identification of deleterious variants that may not be identified by current
542 computational VEP tools. Using transfer learning, our results may also be used to facilitate the
543 analysis of other GPCRs.

544 In conclusion, we have used DMS and cryo-EM to comprehensively map the mutational
545 landscape of the immunomodulatory GPCR P2RY8, advancing understanding of its function.

546 **Methods:**

547 *Cell lines:*

548 HEK 293T (293T), WEHI-231, and parent OCI-Ly8 (Ly8) cell lines were previously obtained
549 from other laboratories and further authentication was not performed. The cell lines were not
550 tested for Mycoplasma contamination. P2RY8 KO Ly8 cells were previously generated as
551 described[29]. The culture medium for Ly8 and WEHI-231 cells was RPMI-1640, 10% FBS, 1x
552 GlutaMax, 10 mM HEPES, 55 uM β-mercaptoethanol, and 50 IU penicillin/streptomycin. Lenti-
553 X 293T cells (Takara) were used to generate lentivirus for transduction of human cells. The
554 culture medium for Lenti-X was DMEM, 10% FBS, 1x GlutaMax, 1 mM sodium pyruvate, 1x
555 MEM non-essential amino acids, 10 mM HEPES, and 50 IU penicillin/streptomycin. Plat-E

556 293T (Plat-E) cells (Cell Biolabs) were used to generate retrovirus for transduction of mouse
557 cells. The culture medium for Plat-E and 293T cells was DMEM, 10% FBS, 1x GlutaMax, 10
558 mM HEPES, and 50 IU penicillin/streptomycin. All cells were maintained in a 37°C humidified
559 incubator, 5% CO_2.

560 *Mice:*

561 Mice used for B cell transfers were C57BL/6J bred in an internal colony and used at 8 to 12
562 weeks of age. For chimeras, donor bone marrow was obtained from C57BL/6J bred internally or
563 purchased from JAX; recipients were CD45.1 B6 (B6.SJL-*Ptprc*a*Pepc*b/BoyCrCrl) mice, bred
564 internally from founders ordered from JAX or purchased from the National Cancer Institute at
565 Charles River at age 7 to 8 weeks, with balanced distribution of experimental groups across these
566 two backgrounds. Mice were allocated to control and experimental groups randomly, and sample
567 sizes were chosen based on previous experience and available co-caged littermates. Animals
568 were housed in a pathogen-free environment in the Laboratory Animal Resource Center at
569 UCSF, and all experiments adhered to ethical principles and guidelines that were approved by the
570 Institutional Animal Care and Use Committee.

571 *Variant pool generation:*

572 The vector for library transduction was created through modification of p_sc-eVIP (p_sc-eVIP
573 was a gift from Jesse Boehm, James T. Neal, and Aviv Regev; Addgene plasmid # 168174)[46].
574 First we removed the puromycin resistance gene by digestion with XhoI, gel purification
575 (Macherey-Nagel Nucleospin kit), blunt end formation withT4 DNA polymerase (NEB), and
576 ligation with Quick Ligase (NEB), transformation into chemically competent bacteria, and
577 plasmid isolation and screening. We then excised P53 and replaced it with PRL-OX56-P2RY8-
578 P2A-GFP. Specifically, two separate PCR reactions were performed using Q5 polymerase (NEB)
579 on MSCV-PRL-OX56-P2RY8-IRES-GFP plasmid (previously described[29]) to produce PRL-
580 OX56-P2RY8-P2A and P2A-GFP fragments with appropriate homology arms for Gibson
581 assembly and thereby cloned into BmtI and PmeI digested plasmid backbone using Gibson
582 assembly kit (NEB). This resulting plasmid is termed POP2E.

583 The variant oligo library was obtained as Site Saturation Variant Library from Twist. The
584 synthesized DNA consisted of the coding sequence for P2RY8 amino acids 2-358 (all codons
585 excepting start and stop codons) along with preceding 35 bp (corresponding to OX56 tag and 5
586 nucleotides in preceding linker) and succeeding 35 bp (corresponding to a portion of P2A
587 sequence). The pools was designed to include all possible missense mutations (a single codon for
588 a given missense amino acid if multiple codons were possible), along with a synonymous codon
589 for all amino acids for which multiple codons exist (that is, all except methionine and
590 tryptophan). Site-directed mutagenesis with the Q5 site-directed mutagenesis kit (NEB) was to
591 modify POP2E by inserting a CTA between P2RY8 and P2A, producing a AvrII restriction site.
592 This new construct was digested with PshAI and AvrII, the non-P2RY8 fragment isolated by gel
593 cleanup (Qiagen Qiaquick Gel Extraction kit), and the oligo pool inserted using using HiFi
594 Assembly kit (NEB): 0.0625 pmol variant oligo library and 0.25 pmol of backbone were
595 combined with 2x master mix for 60 minutes at 50°C. The reaction was cooled on ice then

596 dialyzed for 1 hour on a 0.025 μm MCE membrane (Millipore) floating on ultra-distilled water.
597 Added 2 μL of dialyzed assembly reaction to 50 uL of Endura electrocompetent cells (Biosearch
598 Technologies), incubated on ice for 15 minutes, aliquoted equally to two 0.1 cm cuvettes (Bio-
599 Rad), and electroporated with 1.8 kV, 10 uF, 600 Ω pulse. This was combined with pre-warmed
600 SOC medium, shaken at 37°C for 1 hour, and spread across two 25 cm x 25 cm LB ampicillin
601 plate, with the exception of a small volume used in serial dilutions to determine transformation
602 efficiency. Based on these serial dilutions, the large plates had a total of 1.67×10^6 transformants,
603 for an average of 233 transformants per variant. After overnight growth, colonies were scraped
604 from the plates, pooled, divided in six, processed using HiSpeed Plasmid Midi Prep kit (Qiagen),
605 and repooled.

606 To produce lentivirus, Lenti-X cells were plated into two 10 cm plates, with transfection the
607 following day with cells ~85% confluent. To 3 mL of Opti-MEM, added 90 uL of lipofectamine
608 3000; to another 3 mL Opti-MEM added 13 μg of variant library plasmid, 14 μg psPAX2, 3.5 μg
609 pMD2.G, and 80 μL of P3000 reagent. Combined these after 5 min room temperature incubation.
610 After 25 min further incubation at room temperature, removed culture medium from the Lenti-X
611 plates, then added 5 mL of complete Opti-MEM (Opti-MEM with, 5% FBS, 1x GlutaMax, 1 mM
612 sodium pyruvate, and 1x MEM non-essential amino acids) and 3 mL of the lipofectamine-DNA
613 mixture to each plate. Six hours later removed media and replaced with 6 mL of complete Opti-
614 MEM plus 50 IU penicillin/streptomycin and 1:500 ViralBoost (Alstem). After 24 hours, the
615 media was collected, passed through a 0.45 μm filter, and concentrated 20x using Lenti-X
616 concentrator (Takara) and centrifugation. Four such batches of lentivirus were produced for use
617 in the screen.

618 *Variant pool screening:*

619 The screen was performed using Ly8 cells in which P2RY8 knockout by CRISPR-Cas9 had
620 previously been performed[29]. For each iteration of the screen, 7×10^6 cells were transduced by
621 resuspending cells at 1×10^6 cells mL^{-1} in culture medium and 750 μL of lentivirus diluted in
622 Opti-MEM, such that ~30% of cells were transduced (range 25-34%), indicating an average of
623 294 transduced cells per variant. Post-transduction, the cells was passaged as needed to maintain
624 a cell concentration of 1.5×10^5 to 1.5×10^6 cells mL^{-1} with a total of at least 3×10^6 transduced
625 (GFP$^+$) cells. The four replicates for each assay (surface expression, migration, and proliferation)
626 were drawn from seven independent transductions using four batches of lentiviral library.

627 Sample collection for surface expression assay occurred 5 days after transduction for 3 replicates
628 and 7 days after transduction for 1 replicate. Cells were washed with FACS buffer (1x PBS, 2%
629 FBS, 1 mM EDTA), stained for 30 minutes on ice with 1:100 TruStain FcX block (Biolegend)
630 and 1:200 biotinylated anti-OX56 (Bio-X-Cell) at 40×10^6 cells mL^{-1}, washed with FACS buffer,
631 stained for 30 minutes on ice with 1:400 streptavidin-AF647 (Fisher), with e780 fixable viability
632 dye (eBioscience) added to 1:1500 for last 10 minues, washed with FACS buffer, resuspended in
633 FACS buffer, and sorted using FACSAriaFusion. Gating was FSC-A x SSC-A, singlets by FSC-
634 A x FSC-W, live cells by FSC-A x e780, GFP+, and four bins of OX56 (AF647) expression,
635 containing 20%, 30%, 30%, 20% (Extended Data Fig. 1b). Cells were sorted into 25% FBS in

636 PBS at 4°C. Cells were washed, pelleted, and frozen at -80°C until DNA extraction for
637 processing and sequencing. An average of 2 x 10^6 cells per bin per sort were collected.

638 The collection for proliferation analysis occurred at 3, 5, and12 days after transduction for all
639 four replicates asas well as 7 days after for two replicates and 8 days after for one replicate. (The
640 Enrich2 algorithm can accommodate and account for these differences.) The proportion of GFP$^+$
641 cells was determined by flow cytometry of a small aliquot at the time of collection. Cell aliquots
642 containing an average of 2.3 x 10^6 GFP$^+$ cells (range 1.5-3.1 x 10^6) were washed with PBS,
643 pelleted, and frozen at -80°C until DNA extraction for processing and sequencing.

644 Migration assays occurred 5 days (one replicate), 7 days (two replicates), or 8 days (one
645 replicate) after transduction. In each case, 80 x 10^6 cells were washed with migration medium
646 (RPMI, 0.5% fatty acid-free bovine serum albumin, 1x penicillin/streptomycin), resuspended in
647 migration medium at 1 x 10^7 cells mL^{-1} and resensitized for 15 minutes at 37°C. Migration
648 medium containing 100 ng mL^{-1} recombinant human CXCL12 (Peprotech) and 100 nM GGG
649 (Cayman) was prepared and 600 μL added to each of 80 wells in 24-well tissue culture plates.
650 Transwell inserts (6 mm, 5 uM pore size, Corning) were placed in each well, after which 100 uL
651 resensitized cells (1 x 10^6 cells) were added to the upper chamber. The cells were placed in 37°C,
652 5% CO_2 incubator for 3 hours to allow migration. The transwells were then removed and the
653 cells in the bottom wells were pooled and counted. A small aliquot was also analyzed by flow
654 cytometry to determine the proportion of GFP$^+$ cells. The total number of migrated cells ranged
655 from 10 to 21 x 10^6 cells. In addition, an aliquot containing 2-3 x 10^6 GFP$^+$ cells from the pre-
656 migration input population was also separately collected for each migration. Cells were washed
657 with PBS, pelleted, and frozen at -80°C until DNA extraction for processing and sequencing.

658 *Sequencing library preparation:*

659 Library preparation and sequencing was performed as two batches, with two replicates for each
660 condition per batch. Genomic DNA was isolated using Quick-DNA Miniprep Plus kit (Zymo)
661 per its instructions. DNA was quantified using Qubit (Thermo Fisher Scientific). Initial PCR
662 amplification reactions were set up to amplify P2RY8 coding sequence plus ~150 flanking bp on
663 each end. Each reaction was 50 μL using Q5 High-Fidelity Polymerase (NEB), including 0.5 μL
664 polymerase, 10 μL 5x buffer, 10 μL high GC enhancer, 0.5 μL 20 μM forward primer, 0.5 μL 20
665 μM reverse primer, and 27.5 μL of DNA, up to 1500 ng of DNA per reaction. When possible,
666 number of individual PCR reactions per sample was set to have total template equivalent to 150
667 transduced cells per variant (1.057 x 10^6 transduced cells total); achieved for 26 of 39 samples;
668 variant coverage for the remaining samples was 57x, 66x, 83x, 100x (four samples), 104x, 106x,
669 120x, 124x, 145x, and 146x. PCR conditions were 98°C x 2 min, 19 cycles of (98°C x 10 sec,
670 70°C x 15 sec, 72°C x 45 sec), and 72°C x 2 min. After the PCR was performed, all individual
671 PCR reactions for a given template were pooled. Approximately 5-10% (depending on total
672 number of reactions) of each pooled reaction was loaded onto agarose gel, band of desired size
673 verified using gel electrophoresis, and band then cut out and PCR product isolated using Qiaex II
674 kit (Qiagen). DNA was quantified using Qubit. DNA was diluted as needed and 1 ng was
675 tagmented using Nextera XT Library Prep kit (Illumina) per its instruction, including 12 cycle
676 PCR for adding Illumina adapter sequences. DNA clean up performed using AMPure XP beads

677   (Beckman) using 0.75x volume (to remove fragments <300 bp). Quantification and QC was

678   performed using Qubit and gel electrophoresis including TapeStation high-sensitivity

679   electrophoresis (Agilent). Samples were diluted and pooled in equimolar fashion to 10 nM total.

680   PE300 sequencing was performed on Illumina NovaSeq X Plus at UCSF CAT.

681   *Sequencing analysis:*

682   Fastq files were obtained from UCSF CAT. There was a mean of 6.51×10^7 paired sequences per

683   sample, SD 1.02×10^7, max 8.60×10^7, min 3.72×10^7. Overall quality was evaluated using

684   FastQC[47] (version 0.12.0) (http://www.bioinformatics.babraham.ac.uk/projects/fastqc/). Adapter

685   trimming then performed using BBDuk function of BBTools[48,49] (version 38.18)

686   (https://sourceforge.net/projects/bbmap/). Paired reads were error corrected using BBMerge (also

687   part of BBTools). Reads were then mapped to P2RY8 amplicon reference sequence using

688   BBMap (also part of BBTools). Variants were then called in the mapped SAM file using

689   AnalyzeSaturationMutagenesis function within GATK[50,51] (version 4.5.0.0)

690   (https://gatk.broadinstitute.org/hc/en-us). The utilized output of this analysis was a table

691   containing the read count for each codon for each position in the coding sequence of P2RY8.

692   These tables were then processed using R to filter for only the codons specifically used by Twist

693   in creating the variant oligo pool and formatted as required for analysis by Enrich2[52] (version

694   1.3.1)(https://github.com/FowlerLab/Enrich2/). Enrichment scores were calculated from the

695   processed files, looking at all four replicates concurrently, by weighted least squares method for

696   surface expression and proliferation and log ratios for migration (since only two points). For

697   each sample, the geometric mean of the counts for the 334 synonymous variants had been

698   calculated and was used as the sample WT count for normalization within Enrich2. The Enrich2

699   output was further processed in R, including determination of z-scores for expression, migration,

700   and proliferation for all missense variants based on the standard deviation of the Enrich2 scores

701   for the synonymous variants. Expression-adjusted migration score determined by finding sum of

702   expression and migration mean z-scores for each position, with high expression-adjusted

703   migration score defined as being more than 1.5 times the interquartile-range away the median

704   and having mean migration z-score > 0.75. Variant counts and Enrich2 scores are in

705   Supplemental Table 2. Scripts used for analysis are available on GitHub at

706   https://github.com/yelabucsf/P2RY8_DMS.

707   *ESM1b fine-tuning using P2RY8 DMS data:*

708   ESM1b takes a single amino acid sequence of length L as input and outputs a 20 x L matrix of

709   log-likelihood ratios (LLR) corresponding to the predicted effects of all single amino acid

710   substitutions[6,53]. To improve the predictive power of ESM1b on P2RY8, here we fine tune the

711   model on a randomly chosen subset of the DMS data (e.g., expression z-scores of k variants per

712   position) and use the rest of the DMS data for performance evaluation (test set). This process is

713   repeated N=50 times for each experimental measurement (expression, migration and

714   proliferation) and each training set size with k = 2, 3, 5, 7, 9 and 11 variants per position.

715   Fine-tuning was performed by updating the parameters of the ESM1b model to minimize a

716   masked mean-squared error loss computed between the sampled experimental values and the

717 corresponding model predictions. Before calculating the loss, the sampled experimental values
718 were transformed to match the mean, variance, and the sign of the P2RY8 zero-shot LLRs to
719 enable faster convergence and avoid major changes to the language model logit distribution
720 during training. We further restricted optimization to the language model's final layers,
721 comprising the LM head and the last three embedding layers (~60M trainable parameters), to
722 preserve the broader contextual knowledge acquired during self-supervised pre-training while
723 enabling adaptation to the experimental data.

724 Model optimization was carried out using an AdamW optimizer (with a learning rate of 1e-5 and
725 weight decay of 0.01) alongside a linear warmup schedule for a maximum of 300 optimization
726 steps . To avoid overfitting to the sampled experimental data, we implemented an early stopping
727 strategy. Specifically, for each training set size, we fine-tuned the model on k-1 variants per
728 position and used the remaining one variant per position for validation. Throughout training, the
729 validation set was used to monitor model performance (Spearman correlation between model
730 predictions and experimental measurements), and training was stopped if the validation
731 correlation did not improve over a predefined number of steps (patience = 30 steps).

732 After fine-tuning, the updated model generated revised LLR predictions for all P2RY8 variants.
733 To further refine these predictions, we incorporated a ridge regression step that combined one-
734 hot encoded sequence features with the fine-tuned model scores. This final regression model was
735 trained on the same set of k experimental variants per position (including variants from both
736 training and validation sets) without transforming the experimental values, to provide predictions
737 on the experimentally measured scale (e.g., P2RY8 expression z-scores in the case of the
738 expression DMS screen). We also implemented the augmented one-hot encoded ridge regression
739 model previously described[35], which relies solely on zero-shot model predictions
740 (AlphaMissense and original ESM1b scores), as a baseline to evaluate the performance gains
741 obtained by fine-tuning ESM1b using P2RY8 DMS data.

742 Finally, we tested whether ESM1b fine-tuning on P2RY8 DMS data can improve variant effect
743 predictions for GPR68, a related GPCR with available DMS data. For this task, we fine-tuned
744 ESM1b on P2RY8 as above, using all experimental DMS data (expression z-scores) for training
745 and tested performance on GPR68 (surface expression and ph 5.5 signaling). We tested the
746 performance of two fine-tuned models, one solely relying on the P2RY8 validation set for early
747 stopping and a second one with a hard stop at 50 optimization steps to avoid overfitting. Overall
748 both models generate similar variant effect scores (LLR) when tested on GPR68, with the latter
749 providing a small increase in Spearman correlation compared to the original (zero-shot) ESM1b
750 model.

751 *Individual variant validation:*

752 Specific variants of interest were produced in the POP2E (WT P2RY8) vector by site-directed
753 mutagenesis (Q5 Site-Directed Mutagenesis Kit, NEB). Lentivirus was produced using Lenti-X
754 by same approach as for lentiviral pool (described above) but scaled down to 1-2 wells in a 6-
755 well plate. Ly8 cells were transduced by same approach as lentiviral pool, again scaled down to 1
756 x 10^5 cells in 100 uL in a well in a 96-well plate per transduction.

757 For surface expression, cells were assessed 3 days after transduction. Cells were washed with
758 FACS buffer, stained for 30 minutes on ice with 1:100 TruStain FcX block (Biolegend) and
759 1:200 biotinylated anti-OX56 (Bio-X-Cell), washed twice, stained for 30 minutes on ice in the
760 dark with 1:250 streptavidin-AF647 (Fisher), washed, stained for 10 minutes on ice in dark with
761 1:1500 e780 fixable viability dye (eBiosciences), washed, and resuspended and analyzed on a
762 FACSymphony (BD). An aliquot of untransduced Ly8 cells were used in each experiment to set
763 the GFP$^+$ gate.

764 For proliferation, transduced cells were maintained in wells of a 24-well tissue culture plate. The
765 ratio of GFP$^+$ to GFP$^-$ cells was tracked over time by performing flow cytometric analysis of an
766 aliquot at 3, 5, 7, 10, 13, and 16 days after transduction. Cells were passaged at those same time
767 points.

768 For migration, cells were assayed 5-7 days after transduction. Cells were washed with migration
769 medium (RPMI, 0.5% fatty acid free BSA (Sigma), 10 mM HEPES, and 50 IU
770 penicillin/streptomycin), resuspended at 2×10^6 cells mL^{-1} and resensitized for 10 to 15 minutes
771 at 37°C. Recombinant human CXCL12 (Peprotech) was diluted to 100 ng mL^{-1} in migration
772 medium. GGG was diluted to various concentrations in the CXCL12-containing migration
773 medium; DMSO (the vehicle for the GGG stock solution) was also added to the CXCL12 only
774 condition at a dilution equivalent to the highest GGG concentration used in that experiment. We
775 added 600 μl of these mixtures to a 24-well tissue culture plate. Transwell filters (6 mm insert, 5
776 μm pore size, Corning) were placed on top of each well, and 100 μL of resensitized cells (2×10^5
777 cells) was added to the transwell insert. The plate was placed in a 37°C, 5% CO_2 incubator, and
778 the cells were allowed to migrate for 3 hours, after which the cells in the bottom well were
779 counted by flow cytometry. To determine the degree of migration inhibition, the number of GFP$^+$
780 cells that migrated in each well was normalized to GFP$^-$ cells, and this ratio in turn compared to
781 that for CXCL12 alone.

782 *Proliferation assay with exogenous GGG:*

783 P2RY8 KO Ly8 cells were transduced as described in *Individual variant validation* above.
784 Starting on day 3, GGG (or DMSO as a control) was added to the culture media each day to the
785 final desired concentration (ranging from 1 nM to 1 μM GGG, or 1:1000 DMSO). The ratio of
786 GFP$^+$ to GFP$^-$ cells was tracked over time by flow cytometry at 3, 5, 7, and 10 days after
787 transduction. Cells were passaged at each of those time points as well.

788 *Candidate ligand migration assay:*

789 P2RY8-expressing WEHI-231 cells were produced as previously described[29]. In brief, P2RY8
790 had been cloned into the murine stem cell virus (MSCV)-GFP retroviral vector. The retrovirus
791 was produced using Plat-E cell line. WEHI-231 cells were transduced in a 6 well plate with
792 retroviral supernatant, centrifuged at 1,340 x g for 2 h at room temperature. The supernatant was
793 removed and standard WEHI-231 culture media replaced. This spinfection was repeated 24 h
794 later.

795 Post-transduction cells were washed with migration medium (RPMI, 0.5% fatty acid free BSA
796 (Sigma), 10 mM HEPES, and 50 IU penicillin/streptomycin), resuspended at 2×10^6 cells mL^{-1}
797 and resensitized for 10 to 15 minutes at 37°C. Recombinant human CXCL12 (Peprotech) was
798 diluted to 50 ng mL^{-1} in migration medium. GGG or other candidate ligands were diluted to
799 various concentrations in the CXCL12-containing migration medium. We added 600 μl of these
800 mixtures to a 24-well tissue culture plate. Transwell filters (6 mm insert, 5 μm pore size,
801 Corning) were placed on top of each well, and 100 μL of resensitized cells (2×10^5 cells) was
802 added to the transwell insert. The plate was placed in a 37°C, 5% CO_2 incubator, and the cells
803 were allowed to migrate for 3 hours, after which the cells in the bottom well were counted by
804 flow cytometry. To determine the degree of migration inhibition, the number of GFP+ cells that
805 migrated in each well was normalized to GFP- cells, and this ratio in turn compared to that for
806 CXCL12 alone.

807 *Phospho-flow:*

808 P2RY8 KO Ly8 cells were transduced with variants of interest as described in *Individual variant*
809 *validation* above. Phospho-flow analyses were performed 5 to 7 days after transduction. Cells
810 were washed in migration medium (RPMI, 0.5% fatty-acid free BSA, 10 mM HEPES, and 50 IU
811 penicillin/streptomycin). They were then resuspended in migration medium at 5×10^6 cells mL^{-1}
812 and resensitized at 37°C for 12 minutes. At that time 100 μL (5×10^5) cells were diluted to 200
813 uL in 5 mL polystyrene round bottom tube with indicated combinations of 100 nM GGG and 100
814 ng mL^{-1} CXCL12 and incubated in 37°C water bath for 5 minutes. Afterward, 22 uL of 16%
815 paraformaldehyde was added to each tube and cells fixed at room temperature for 10 minutes,
816 centrifuged, supernatant removed, and 1 mL of cold methanol added while vortexing. The
817 samples were placed at -20°C for 1-2 nights (consistent within given experiment). They were
818 then washed three times with FACS buffer and divided into three equal aliquots, one of which
819 was used for pAkt and one of which was used for pErk. They were blocked for 20 minutes at
820 room temperature with 5% normal goat serum and 1:100 human Fc block (Trustain FcX,
821 Biolegend) and stained at room temperature for 1 hour with a 1:100 dilution of rabbit anti-pAkt
822 (Cell Signaling Technology, Ser473, clone D9E) or 1:100 rabbit anti-pErk1/2 (Cell Signaling
823 Technology, T202/T204, #9102). They were washed twice in FACS buffer, stained for 1 h at
824 room temperature with 1:300 streptavidin-AF647 and 1:250 anti-GFP (Biolegend, clone
825 FM264G), washed with FACS buffer, and analyzed.

826 *NanoBit β-arrestin assay:*

827 This assay was performed in 293T cells. β2AR-LgBiT and β-Arr2-SmBiT plasmids had
828 previously been generated[54]. The β2AR-LgBiT plasmid was digested with EcoRI and BmtI and
829 β2AR replaced with P2RY8 coding sequence, either WT or with V29W, K180I, W181M, or
830 L220Y missense variants, using PCR on the plasmids previously generated for *Individual variant*
831 *validation*. On day 0, 293T cells were plated into 6-well plate. On Day 1, with cells now ~80%
832 confluent, cells were transfected. Specifically, to 250 μL Opti-MEM added 400 ng of desired
833 LgBiT construct, 100 ng of β-Arr2-SmBiT, and 1.5 μL of Trans-IT 2020 (Mirus) and gently
834 mixed. After 25 min incubation at room temperature, this was added dropwise to well of the
835 293T cells. On Day 2, culture medium was removed. Cells were dissociated from plate using

836   PBS with 0.5 mM EDTA, washed, and counted. Cells were resuspended at 4 x 10^5 cells mL^{-1} in

837   assay solution (Hanks' balanced salt solution with 20 mM HEPES) and 100 µL (4 x 10^4 cells)

838   added to wells in 96-well white flat-bottom plate. To this, added 50 µL of 15 µM coelenterazine

839   h (Nanolight). After 10 minutes, measured baseline luminescence. Then added 50 µL of desired

840   GGG dilution in assay solution with 5 µM coelenterazine h to yield final concentrations ranging

841   from 100 pM to 10 µM as well as a DMSO (vehicle) condition. After 10 minutes, measured

842   luminescence again. For analysis, looked at ratio of post-GGG signal to baseline signal,

843   normalized to DMSO condition ratio.

844   *TRUPATH BRET trimeric G protein assay:*

845   This assay was performed in 293T cells. To start, 5 x 10^5 cells were plated per well in a 6-well

846   plate. The next day, they were transfected. Specifically, to 250 µL of Opti-MEM, added 150 ng

847   of P2RY8 WT, P2RY8 variant, or GFP only plasmid (same POP2E original or modified as used

848   in *Individual variant validation* above), 100 ng pcDNA5/FRT/TO-GAlpha13-RLuc8, 100 ng

849   pcDNA3.1-Beta3, 100 ng of pcDNA3.1-GGamma9-GFP2, and 1.35 µL of Trans-IT 2020 reagent

850   (Mirus) and gently mixed; after 25 minutes incubation at room temperature, this was added

851   dropwise to well of the 293T cells. pcDNA5/FRT/TO-GAlpha13-RLuc8, pcDNA3.1-Beta3, and

852   pcDNA3.1-GGamma9-GFP2 were gifts from Bryan Roth, Addgene plasmid #140986, 140988,

853   and 140991[42]. The next day, 96-well white flat-bottom plates (Greiner Bio-One) were treated for

854   2 hours with 50 µg mL^{-1} poly-D-lysine (diluted from 1 mg mL^{-1}, EMD-Millipore) in sterile ultra-

855   distilled water, washed once with water, then dried for 1 hour. Culture medium removed from the

856   transfected cells, cells were dissociated from plate using PBS with 0.5 mM EDTA, washed,

857   resuspended at 2.67 x 10^5 cells mL^{-1} in culture medium, and 150 µL (4 x 10^4 cells) aliquoted per

858   well of poly-D-lysine treated plate. The following day, the plate was centrifuged at 500 x g for 1

859   min, culture medium removed, and 60 µL of assay medium (Hanks' balanced salt solution plus

860   20 mM HEPES) was added to each well. From 2.5 mM stock of coelenterazine 400a (Nanolight),

861   a 50 µM dilution in assay buffer was made. In addition, desired dilutions of GGG in assay were

862   prepared (at four times the ultimately desired concentration). Transported cells on ice to building

863   with BRET-capable plate reader, plate again centrifuged 500 x g for 1 min, and 10 µL of

864   coelenterazine working solution was added. After 10 minutes, 30 µL of desired GGG solution

865   was added, yielding final concentrations ranging from 100 pM to 10 µM; there was also a 1:100

866   DMSO (vehicle) condition. After 8 minutes, loaded on plate reader and measured 420 ± 20 nm

867   and 515 ± 20 nm for luciferase and GFP, respectively. Measured 6 times, each spaced by 3

868   minutes. For analysis, calculated luminescence to GFP ratio for each time point and determined

869   mean across the six measurements.

870   *B cell transduction, transfer, and analysis:*

871   P2RY8 was previously cloned into the MSCV-GFP retroviral vector as described[29]. The GFP was

872   replaced by digestion of MSCV-P2RY8-IRES-GFP with BstXI and PacI and insertion of TagBFP

873   PCR product using HiFi DNA Assembly Kit (NEB). The WT P2RY8 MSCV was digested with

874   BglII and NotI and K180I or W181M P2RY8 PCR products (from the constructs detailed in

875   *Individual variant validation* above) were inserted using HiFi DNA Assembly Kit (NEB).

876   Retrovirus encoding P2RY8-TagBFP, K180I-GFP, and W181M-GFP were produced using Plat-E

packaging line as described[28]. EasySep kits were used to enrich B cells from mouse spleens by removing T cells with biotin-conjugated anti-CD3ε (Biolegend, clone 145-2C11) and streptavidin-conjugated beads (EasySep Streptavidin RapidSpheres). B cells were cultured in complete RPMI (10% FBS, 10 mM HEPES, 1x GlutaMax, 50 IU penicillin/streptomycin, and 55 μM β-mercaptoethanol) along with 25 μg mL^{-1} (1:4000 dilution) anti-CD180 (BD Biosciences, clone RP/14).

Transduction was performed 24 hours after activation. Plates were centrifuged and culture supernatant was saved. Retroviral supernatants were thawed from -80°C and HEPES added to 20 mM and polybrene (EMD Millipore) added to 2 μg mL^{-1}. This was used to spinfect the cells for 2 hours at room temperature, centrifuging at 2500 rpm. The viral supernatant was then aspirated and half the original culture medium was replaced along with an equal volume of culture medium with freshly added anti-CD180. The spinfection was repeated a second time 24 hours later.

Twenty-four hours after the second transduction, cells were collected from the plate, washed twice, and placed on ice. A small aliquot was analyzed by flow cytometry to determine the proportion of transduced (GFP$^+$ or TagBFP$^+$) cells. Cells were diluted and pooled (WT P2RY8 and K180I P2RY8 or WT P2RY8 and W181M P2RY8) to desired ratio and injected IV into recipient mice, who had been immunized intraperitoneally 7 days earlier with 2 x 10^8 SRBCs. Mice received 4-5 x 10^6 WT-TagBFP$^+$ cells and 7-10 x 10^6 K180I-GFP$^+$ or W181M-GFP$^+$ cells.

Mice were analyzed 24 hours after transfer. Spleens were harvested, cut into 4-5 sections, and fixed for 30 minutes in 4% paraformaldehyde in PBS at 4°C, washed, then dehydrated overnight at 4°C in 30% sucrose solution. Spleen segments were placed in cassette with OCT medium (Sakura), flash frozen, and placed at -80°C for storage. Cryostat was used to cut 7 μm sections. These were dried at room temperature for one hour then rehydrated with PBS 0.1% fatty-acid-free (FAF) BSA for 10 minutes. They were stained overnight at 4°C with primary stain of PBS 0.1% FAF-BSA, 1:100 normal mouse serum, 1:100 anti-GFP AF488 (rabbit polyclonal, Invitrogen A21311), 1:100 anti-CR1 (CD35)-biotin (BD 553816, clone 8C12), 1:100 anti-IgD AF647 (Biolegend 405708, clone 11-26c2a), and 1:200 or 1:250 anti-TagFP AZ568 (NanoTag N0502-AF568). Cells were washed 3 times with PBS 0.1% FAF-BSA then secondary stain was PBS 0.1% FAF-BSA, 1:100 normal mouse serum, 1:200 streptavidin-AMCA for 1 hour at room temperature. Cells were washed 2 times with PBS 0.1% FAF-BSA, once with PBS, then cover slip affixed using Fluoro-Mount, allowed to harden at 4 C for one hour. Images were acquired using Zeiss AxioObserver Z1 inverted microscope.

Initial image processing performed in ZEN (Zeiss): AMCA channel black/white rescaled from 0-16,034 to 1,596-16,034 for all images obtained. AF555 channel black/white rescaled from 0-16,034 to 1,047-9,052 all images in figures. Further analysis performed using Fiji[55]. Follicles were cropped from larger images and regions of interest containing GCs defined. Using consistent thresholds across images, GFP and BFP signal was made binary and Analyze Particles function (size 10-150 μm^2, circularity 0.3-1) used to count cells within follicles and within subsections of follicles coinciding with GCs. Analysis included at least 45 GCs from each mouse.

918 *Bone marrow chimera generation and analysis:*

919 Mice to be used as bone marrow (BM) donors (C57BL/6J, 8-12 weeks old) were injected
920 intraperitoneally with 3 mg 5-fluorouracil (Sigma). BM was collected after 4 days and cultured
921 in DMEM containing 15% FBS, penicillin (50 IU mL^{-1}), streptomycin (50 μg mL^{-1}), and 10 mM
922 HEPES, supplemented with 250 ng mL^{-1} IL-3, 50 ng mL^{-1} IL-6, and 100 ng mL^{-1} SCF
923 (Peprotech). Cells were transduced with MSCV-EV-GFP, MSCV-P2RY8(WT)-GFP, MSCV-
924 P2RY8(K180I)-GFP, or MSCV-P2RY8(W181M)-GFP) on days 1 and 2 using viral supernatant
925 concentrate thawed, diluted to original concentration with DMEM, 10% FBS, 10 mM HEPES,
926 and 4 ug mL^{-1} polybrene and transduction performed via 2 hr centrifugation at 2400 rpm at 32°C,
927 followed by replacement with culture media. Recipient CD45.1 B6 mice, age 7-10 weeks, were
928 lethally irradiated with 900 rads (evenly split dose separated by 3 h) and then injected IV with
929 relevant transduced BM cells. For every 3-3.5 recipient mice, 1 donor mouse was used. Mice
930 were analyzed 10-12 weeks after reconstitution.

931 For analysis, spleen, mesenteric lymph nodes, and Peyer's patches were isolated. Mesenteric
932 lymph nodes and Peyer's patches were digested for 20 min at 37°C, shaking, in 1 mg mL^{-1}
933 collagenase VIII (Sigma) in RPMI with 10% FBS. After mashing, straining, and washing, tissues
934 were blocked for 10 min with 1:100 Fc block (Bio-X-Cell) in FACS buffer (PBS, 2% FBS, 1
935 mM EDTA), then stained for 30 minutes on ice with anti-CD45.2 PE (Biolegend 109808), anti-
936 CD45.1 APC (Cytek 20-0453-U100), anti-GL7 PacBlue (Biolegend 144614), anti-IgD PerCP-
937 Cy5.5 (Biolegend 405710), anti-CD95 PE-Cy7 (Fisher 557653), anti-B220 BV785 (Biolegend
938 103246), and, for spleen, also anti-CD8a BV510 (Biolegend 100752), anti-CD11b BV570
939 (Biolegend 101233), anti-CD4 BV711 (Biolegend 100447), and anti-CD3ε AF700 (Biolegend
940 152316), all 1:200. Cells were washed, stained for 10 minutes with e780 fixable viability dye
941 (eBiosciences), and washed again. Cells were then analyzed on FACSymphony.

942 *Expression and purification of P2RY8-miniG$_{13}$ protein:*

943 Human P2RY8 (Uniprot: Q86VZ1) was cloned into pCDNA-Zeo-TetO, a custom pcDNA3.1
944 vector containing a tetracycline-inducible gene expression cassette[56]. The resulting P2RY8
945 construct comprised an N-terminal influenza haemagglutinin signal sequence followed by a M1-
946 FLAG (DYKDDDD) epitope tag. The P2RY8 construct was furthermore fused at the C-terminus
947 to the miniGα$_{13}$ protein via a linker sequence containing a human rhinovirus 3C (HRV 3C)
948 protease cleavage site. The resulting P2RY8–miniGα$_{13}$ construct was transiently transfected into
949 inducible Expi293F TetR cells (unauthenticated and untested for mycoplasma contamination;
950 Thermo Fisher) using the ExpiFectamine 293 Transfection Kit (Thermo Fisher) following the
951 manufacturer's instructions. After 16 h, protein expression was induced with 1 μg ml^{-1}
952 doxycycline hyclate (Sigma Aldrich), and the culture was placed in a shaking incubator
953 maintained at 37°C and 8% CO$_2$. After 36 h, cells were harvested by centrifugation at 4,000 x g
954 and stored at −80°C.

955 For receptor purification, cells were thawed and resuspended in lysis buffer comprising 20 mM
956 HEPES pH 7.50, 10 μM S-geranylgeranyl-L-glutathione (GGG, Cayman Chemical), 100 μM
957 tris(2-carboxyethyl)phosphine (TCEP; Fischer Scientific), and a Pierce protease inhibitor tablet

958 (Thermo Scientific). Cells were lysed by stirring for 15 min at 4 °C and harvested by
959 centrifugation at 16,000 x g for 15 min. To increase the fraction of GGG-bound P2RY8, we also
960 reconstituted GGG into detergent to overcome its low solubility. 25 mg of GGG and 1.5 g of
961 lauryl maltose neopentyl glycol (L-MNG; Anatrace) was dissolved in methanol and allowed to
962 mix for 10 min at RT. The LMNG-GGG mixture was was placed under an Argon stream
963 evaporated to dryness followed by vaccuum dessication overnight. The dry LMNG-GGG
964 mixture was resuspended in 20 mM HEPES pH 7.50, 100 mM NaCl by sonication. Cell pellet
965 was dounce-homogenized in ice-cold solubilization buffer comprising 50 mM HEPES, pH 7.5,
966 150 mM NaCl, 1% (w/v) lauryl maltose neopentyl glycol (L-MNG; Anatrace) containing 3 mol%
967 GGG, 0.1% (w/v) cholesteryl hemisuccinate (CHS, Steraloids), 5 mM adenosine 5′-triphosphate
968 (ATP; Fischer Scientific), 2 mM $MgCl_2$, 100 µM TCEP, 10 µM GGG, and a Pierce protease
969 inhibitor tablet (Thermo Scientific). The sample was stirred for 1 h at 4°C, and the detergent-
970 solubilized fraction was clarified by centrifugation at 20,000 x g for 30 min. The detergent-
971 solubilized sample was supplemented with 4 mM $CaCl_2$ and incubated in batch with homemade
972 M1-FLAG-antibody conjugated CNBr-Sepharose under slow rotation for 1 h at 4 °C. The
973 P2RY8-bound resin was transferred to a glass column and washed with 20 ml of ice-cold buffer
974 comprising 50 mM HEPES, pH 7.5, 150 mM NaCl, 0.1% (w/v) L-MNG containing 3 mol%
975 GGG, 0.01% (w/v) CHS, 5 mM ATP, 2 mM $CaCl_2$, 2 mM $MgCl_2$, 100 µM TCEP. This was
976 followed by 10 column volumes of ice-cold 50 mM HEPES, pH 7.5, 150 mM NaCl, 0.0075%
977 (w/v) L-MNG containing 3 mol% GGG, 0.0025% (w/v) glyco-diosgenin (GDN; Anatrace),
978 0.001% (w/v) CHS, 2 mM CaCl2, 100 µM TCEP, and 10 µM GGG. Receptor-containing
979 fractions were eluted with ice-cold 20 mM HEPES, pH 7.5, 150 mM NaCl, 0.0075% (w/v) L-
980 MNG containing 3 mol% GGG, 0.0025% (w/v) GDN, 0.001% (w/v) CHS, 5 mM EDTA,
981 0.2 mg ml^{-1} FLAG peptide, 100 µM TCEP, and 10 µM GGG. Fractions containing P2RY8–
982 miniGα_{13} were concentrated in a 50-kDa MWCO spin filter (Amicon) and purified over a
983 Superdex 200 Increase 10/300 GL (Cytiva) size-exclusion chromatography (SEC) column, which
984 was equilibrated with 20 mM HEPES, pH 7.5, 150 mM NaCl, 0.0075% (w/v) L-MNG containing
985 3 mol% GGG, 0.0025% (w/v) GDN, 0.001% (w/v) CHS, 100 µM TCEP, and 10 µM GGG.
986 Fractions containing monodisperse P2RY8–miniGα_{13} were combined and concentrated in a 50-
987 kDa MWCO spin filter before complexing with G$\beta_1\gamma_2$.

988 *Expression and purification of G$\beta_1\gamma_2$:*

989 Purified G$\beta_1\gamma_2$ was generated as described previously[57]. Briefly, a baculovirus was generated in
990 Spodoptera frugiperda Sf9 insect cells (unauthenticated and untested for mycoplasma
991 contamination, Expression Systems) using the pVLDual expression vector encoding both human
992 Gβ_1 subunit with a HRV 3C cleavable N-terminal 6xHis-tag and the untagged human Gγ_2
993 subunit. G$\beta_1\gamma_2$ was expressed in Trichoplusia ni Hi5 insect cells (unauthenticated and untested
994 for mycoplasma contamination, Expression Systems) by infection with G$\beta_1\gamma_2$-baculovirus at a
995 density of 3.0×10^6 cells ml^{-1} and grown for 48 h at 27°C with 130 r.p.m. shaking. Harvested
996 cells were resuspended in lysis buffer comprised of 20 mM HEPES, pH 8.0, 5 mM β-
997 mercaptoethanol (β-ME), 20 µg ml^{-1} leupeptin, and 160 µg ml^{-1} benzamidine. Lysed cells were
998 pelleted at 20,000 x g for 15 min, and solubilized with 20 mM HEPES, pH 8, 100 mM sodium
999 chloride, 1% (w/v) sodium cholate (Sigma Aldrich), 0.05% (w/v) n-dodecyl-β-d-

1000   maltopyranoside (DM; Anatrace) and 5 mM β-ME. Detergent-solubilized Gβ$_1$γ$_2$ was clarified by

1001   centrifugation at 20,000 x g for 30 min and was then incubated with HisPur Ni-NTA resin

1002   (Thermo Scientific) under slow rotation for 1.5 h at 4°C. Gβ$_1$γ$_2$-bound resin was transferred to a

1003   glass column and washed extensively. Detergent was exchanged on-column to 0.1% (w/v) L-

1004   MNG and 0.01% (w/v) CHS, and Gβ$_1$γ$_2$ was eluted with 20 mM HEPES pH 7.50, 100 mM NaCl,

1005   0.1% (w/v) L-MNG, 0.01% (w/v) CHS, 300 mM imidazole, 1 mM DL-dithiothreitol (DTT),

1006   20 µg ml^{-1} leupeptin and 160 µg ml^{-1} benzamidine. Gβ$_1$γ$_2$-containing fractions were pooled and

1007   supplemented with homemade 3C protease before overnight dialysis in buffer comprised of

1008   20 mM HEPES, pH 7.50, 100 mM NaCl, 0.02% (w/v) L-MNG, 0.002% (w/v) CHS, 1 mM DTT

1009   and 10 mM imidazole. Cleaved Gβ$_1$γ$_2$ was isolated by reverse Ni-NTA, and dephosphorylated by

1010   treatment with lambda phosphatase (New England Biolabs), calf intestinal phosphatase (New

1011   England Biolabs) and antarctic phosphatase (New England Biolabs) for 1 h at 4 °C. The

1012   geranylgeranylated Gβ$_1$γ$_2$ heterodimer was isolated by anion exchange chromatography using a

1013   MonoQ 4.6/100 PE (Cytiva) column, before overnight dialysis in 20 mM HEPES, pH 7.5,

1014   100 mM NaCl, 0.02% (w/v) L-MNG and 100 µM TCEP. The final sample was concentrated on a

1015   3-kDa MWCO spin filter (Amicon), and 20% (v/v) glycerol was added before flash freezing in

1016   liquid N2 for storage at −80°C.

1017   *Preparation of the active-state of P2RY8-G$_{13}$ complex:*

1018   To prepare the P2RY8–G$_{13}$ complex, a twofold molar excess of purified Gβ$_1$γ$_2$ was added to

1019   SEC-purified P2RY8–miniGα$_{13}$ followed by overnight incubation on ice. The sample was

1020   purified on a Superdex 200 Increase 10/300 GL SEC column, equilibrated with 20 mM HEPES,

1021   pH 7.5, 150 mM NaCl, 0.0075% (w/v) L-MNG containing 3 mol% GGG, 0.0025% (w/v) GDN,

1022   0.001% (w/v) CHS and, 30 µM GGG. Fractions containing the monomeric P2RY8–G13

1023   heterotrimeric complex were concentrated on a 50-kDa MWCO spin filter (Amicon)

1024   immediately before cryo-EM grid preparation.

1025   *Cryo-EM vitrification, data collection, and processing:*

1026   2.75 µl of the purified P2RY8–G13 complex was applied at 1.4 mg ml^{-1} to glow-discharged 300

1027   mesh R1.2/1.3 UltrAuFoil Holey gold grids (Quantifoil). Grids were plunge-frozen in liquid

1028   ethane using a Vitrobot Mark IV (Thermo Fisher) with a 10-s hold period, blot force of 0, and

1029   blotting time varying between 1.5 and 3.0 s while maintaining 100% humidity and 4°C. Vitrified

1030   grids were clipped with Autogrid sample carrier assemblies (Thermo Fisher) immediately before

1031   imaging. Movies of P2RY8–G$_{13}$ embedded in ice were recorded on a 300 kV FEI Titan Krios

1032   microscope equipped with a Falcon 4i camera (Thermo Scientific, located at the HHMI Janelia

1033   Research Campus). A nominal magnification of × 130,000 was used in resolution mode with a

1034   physical pixel size of 0.94 Å per pixel, and movies were recorded with a total exposure of

1035   50 e− Å^{-2}. Movies (n = 12,053) were imported into cryoSPARC (Structura Biotechnology) with

1036   80 EER fractions, motion-corrected micrographs were generated with the patch motion correct

1037   tool beofre calculation of patch contrast transfer functions (patch CTFs). A threshold of CTF fit

1038   resolution of more than 6 Å was used to exclude low-quality micrographs. Particles were

1039   template picked using a 20 Å low-pass-filtered model that was generated ab initio from data

1040   collected during earlier screening sessions on a 200-kV Glacios microscope located at UCSF.

1041   Particles (n = 10,117,438) were extracted with a box size of 288 pixels binned to 72 pixels and

1042   sorted by two rounds of 2D classification. The resulting 2,352,975 particles were sorted by ab

1043   initio 3D reconstruction with two classes, re-extracted with a box size of 288 pixels binned to

1044   144 pixels, and sorted by additional two rounds of ab initio 3D construction. Particles

1045   (n = 799,516) were extracted with an unbinned box size of 288 pixels and were subjected to non-

1046   uniform refinement followed by local refinement using a mask covering only the 7TM domain of

1047   P2RY8. Particles were further sorted by two rounds of 3D classification using 4 classes and a

1048   filter resolution of 3.00 Å and 2.75 Å respectively. The resulting 90,243 particles were subjected

1049   to non-uniform refinement followed by local refinement using an inclusion mask covering the

1050   7TM domain, using poses/shift Gaussian priors with standard deviation of rotational and shift

1051   magnitudes limited to 1° and 1 Å, respectively.

1052   *Model building and refinement:*

1053   Model building and refinement were carried out using a starting model based on the AlphaFold2

1054   predicted structure of P2RY8 (Uniprot: Q86VZ1), the deposited structure of $G\alpha_{13}$ (PDB code:

1055   7T6B)[58], and the deposited structure of $G\beta_1\gamma_2$ (PDB code: 8F76)[57] which were fitted into the

1056   P2RY8–G_{13} map using UCSF ChimeraX. A draft model was generated using ISOLDE[59] and was

1057   further refined by iterations of real-space refinement in Phenix v1.20[60] and manual refinement in

1058   Coot v0.8.9.2[61]. The GGG model and rotamer library were generated with the eLBOW

1059   extension[62] in Phenix and docked using Coot. The resulting model was extensively refined in

1060   Phenix and map-model validations were carried out using Molprobity v4.5 and EMRinger[63].

1061   *Chemical synthesis:*

1062   GGG used in WEHI migration assay was synthesized in house as previously described[29]. GGG

1063   for all other assays was purchased from Cayman Chemical and resuspended in DMSO at 1 mM

1064   to form stock solution. Leukotriene C_4 was also purchased from Cayman Chemical.

1065   Synthesis of other glutathione conjugates followed similar approach to GGG[29]. Compound 1

1066   refers to S-octane-L-glutathione, compound 2 refers to S-hexadecane-L-glutathione, compound 3

1067   refers to S-isoprenyl-L-glutathione, and compound 4 refers to S-farnesyl-L-glutathione. Unless

1068   otherwise stated, all reagents were purchased from MilliporeSigma. Briefly, 20 mg (1 eq.) of

1069   farnesol (for compound 4) was stirred in 1 ml of dry DCM under an atmosphere of nitrogen at

1070   room temperature. Triphenylphospine (1.3 eq.) was added, followed by carbon tetrabromide (1.3

1071   eq.), and the reaction was stirred for a further 2–4 hours at room temperature. After

1072   concentrating the crude reaction under reduced pressure, a small volume of n-hexane was added

1073   and the resulting precipitate removed by filtration. Concentration, precipitation and filtration

1074   was repeated once again and the concentrated filtrate used in the next step without further

1075   purification.

1076   Glutathione (1.1 eq) was dissolved in the minimal volume of 2 M NaOH, and ethanol added until

1077   the solution started to become cloudy. Either the compound generated in the first step (for

1078   compound 4), or 1-bromooctane, 1-bromohexadecane, or 3,3-Dimethylallyl bromide (for

1079   compounds 1, 2, and 3) (1 eq.) was added dropwise and the reaction stirred at room temperature

1080   overnight. The pH of the reaction mixture was reduced to 2 by addition of 1 M HCl, and the

1081 reaction cooled in an ice bath until a precipitate formed. This precipitate was collected by
1082 filtration, washed with a small volume of ice-cold ethanol and then ice-cold water, and dried to
1083 yield the final glutathione conjugate.

1084 *Statistics and graphing:* Bar and line graphs and included statistics made using Prism
1085 (GraphPad). Other plots and statistics using R version 4.3.0 in RStudio 2023.03.0+386, relevant
1086 packages tidyverse 2.0.0, ggplot2 3.4.2. P2RY8 structure analysis using ChimeraX version
1087 1.8[64,65]. Regression analysis using Jupyter Notebook 6.5.4, Python 3.11.4, numpy 1.24.3, pandas
1088 1.5.3, scipy 1.10.1, and sklearn 1.5.2.

Data Availability:

1090 Sequencing data from the deep mutational scan have been deposited in the NCBI Sequence Read
1091 Archive under BioProject PRJNA1179413 and are publicly available as of the date of
1092 publication. Coordinates for the P2RY8-Gα_{13} complex have been deposited in the RCSB Protein
1093 Data Bank under accession codes 9ECJ. EM density map for the P2RY8-Gα_{13} complex has been
1094 deposited in the Electron Microscopy Data Bank under accession codes EMD-47912 (full map)
1095 and EMD-47914 (7TM map). *Previously available data:* Germline variants from gnomAD[2]
1096 v4.0.0 at https://gnomad.broadinstitute.org. Non-hematologic cancer variants and some DLBCL
1097 / Burkitt lymphoma variants from COSMIC[45] at https://cancer.sanger.ac.uk/cosmic, accessed
1098 Feb. 1, 2024.

Code Availability:

1100 Analysis code are available on GitHub at https://github.com/yelabucsf/P2RY8_DMS. Any
1101 additional information required to reanalyze the data reported in this paper is available from the
1102 lead contact upon request.

Acknowledgments:

1120 operation and data collection. Molecular graphics and analyses performed with UCSF
1121 ChimeraX, developed by the Resource for Biocomputing, Visualization, and Informatics at the
1122 University of California, San Francisco, with support from National Institutes of Health R01-
1123 GM129325 and the Office of Cyber Infrastructure and Computational Biology, National Institute
1124 of Allergy and Infectious Diseases. We thank Zachary Earley for assistance with murine tissue
1125 analysis.

Author contributions:

1127 T.N.L., C.B.B., A.M., J.C.G., and C.J.Y. conceived and designed this study. T.N.L. performed
1128 DMS and follow-up experiments, performed most VEP analyses, and took lead in writing the
1129 paper. C.B.B. performed cryo-EM sample preparation and data analysis. J.C.G., C.J.Y, A.M., and
1130 C.B.B. co-wrote the paper. T.D. and V.N.. performed ESM1b fine-tuning and some related
1131 analysis. F.D.W. synthesized candidate ligands. E.L. performed migration assay with candidate
1132 ligands. J.A. participated in creating the mouse chimeras. Y.X. participated in cloning and
1133 plasmid preparation. A.S. participated in NanoBit and TRUPATH assays and cloning and
1134 plasmid preparation. T.M. and N.B. assisted with VEP analysis.

References:

1145 1. Bycroft, C., Freeman, C., Petkova, D., Band, G., Elliott, L.T., Sharp, K., Motyer, A.,
1146   Vukcevic, D., Delaneau, O., O'Connell, J., et al. (2018). The UK Biobank resource with deep
1147   phenotyping and genomic data. Nature *562*, 203–209. https://doi.org/10.1038/s41586-018-
1148   0579-z.

1149 2. Karczewski, K.J., Francioli, L.C., Tiao, G., Cummings, B.B., Alföldi, J., Wang, Q., Collins,
1150   R.L., Laricchia, K.M., Ganna, A., Birnbaum, D.P., et al. (2020). The mutational constraint
1151   spectrum quantified from variation in 141,456 humans. Nature *581*, 434–443.
1152   https://doi.org/10.1038/s41586-020-2308-7.

1153 3. Medina-Carmona, E., Betancor-Fernández, I., Santos, J., Mesa-Torres, N., Grottelli, S.,
1154   Batlle, C., Naganathan, A.N., Oppici, E., Cellini, B., Ventura, S., et al. (2019). Insight into
1155   the specificity and severity of pathogenic mechanisms associated with missense mutations
1156   through experimental and structural perturbation analyses. Hum Mol Genet *28*, 1–15.
1157   https://doi.org/10.1093/hmg/ddy323.

4. Malhotra, S., Alsulami, A.F., Heiyun, Y., Ochoa, B.M., Jubb, H., Forbes, S., and Blundell, T.L. (2019). Understanding the impacts of missense mutations on structures and functions of human cancer-related genes: A preliminary computational analysis of the COSMIC Cancer Gene Census. PLoS One *14*, e0219935. https://doi.org/10.1371/journal.pone.0219935.

5. Martínez-Jiménez, F., Muiños, F., Sentís, I., Deu-Pons, J., Reyes-Salazar, I., Arnedo-Pac, C., Mularoni, L., Pich, O., Bonet, J., Kranas, H., et al. (2020). A compendium of mutational cancer driver genes. Nat Rev Cancer *20*, 555–572. https://doi.org/10.1038/s41568-020-0290-x.

6. Brandes, N., Goldman, G., Wang, C.H., Ye, C.J., and Ntranos, V. (2023). Genome-wide prediction of disease variant effects with a deep protein language model. Nat Genet *55*, 1512–1522. https://doi.org/10.1038/s41588-023-01465-0.

7. Cheng, J., Novati, G., Pan, J., Bycroft, C., Žemgulytė, A., Applebaum, T., Pritzel, A., Wong, L.H., Zielinski, M., Sargeant, T., et al. (2023). Accurate proteome-wide missense variant effect prediction with AlphaMissense. Science *381*, eadg7492. https://doi.org/10.1126/science.adg7492.

8. Gao, H., Hamp, T., Ede, J., Schraiber, J.G., McRae, J., Singer-Berk, M., Yang, Y., Dietrich, A.S.D., Fiziev, P.P., Kuderna, L.F.K., et al. (2023). The landscape of tolerated genetic variation in humans and primates. Science *380*, eabn8153. https://doi.org/10.1126/science.abn8197.

9. Stein, D., Kars, M.E., Wu, Y., Bayrak, Ç.S., Stenson, P.D., Cooper, D.N., Schlessinger, A., and Itan, Y. (2023). Genome-wide prediction of pathogenic gain- and loss-of-function variants from ensemble learning of a diverse feature set. Genome Med *15*, 103. https://doi.org/10.1186/s13073-023-01261-9.

10. Ostroverkhova, D., Sheng, Y., and Panchenko, A. (2024). Are Next-Generation Pathogenicity Predictors Applicable to Cancer? J Mol Biol *436*, 168644. https://doi.org/10.1016/j.jmb.2024.168644.

11. Fowler, D.M., and Fields, S. (2014). Deep mutational scanning: a new style of protein science. Nat Methods *11*, 801–807. https://doi.org/10.1038/nmeth.3027.

12. Kinney, J.B., and McCandlish, D.M. (2019). Massively Parallel Assays and Quantitative Sequence-Function Relationships. Annu Rev Genomics Hum Genet *20*, 99–127. https://doi.org/10.1146/annurev-genom-083118-014845.

13. Tabet, D., Parikh, V., Mali, P., Roth, F.P., and Claussnitzer, M. (2022). Scalable Functional Assays for the Interpretation of Human Genetic Variation. Annu Rev Genet *56*, 441–465. https://doi.org/10.1146/annurev-genet-072920-032107.

14. Fowler, D.M., Adams, D.J., Gloyn, A.L., Hahn, W.C., Marks, D.S., Muffley, L.A., Neal, J.T., Roth, F.P., Rubin, A.F., Starita, L.M., et al. (2023). An Atlas of Variant Effects to understand the genome at nucleotide resolution. Genome Biol *24*, 147. https://doi.org/10.1186/s13059-023-02986-x.

15. Bjarnadóttir, T.K., Gloriam, D.E., Hellstrand, S.H., Kristiansson, H., Fredriksson, R., and Schiöth, H.B. (2006). Comprehensive repertoire and phylogenetic analysis of the G protein-coupled receptors in human and mouse. Genomics *88*, 263–273. https://doi.org/10.1016/j.ygeno.2006.04.001.

16. Hauser, A.S., Attwood, M.M., Rask-Andersen, M., Schiöth, H.B., and Gloriam, D.E. (2017). Trends in GPCR drug discovery: new agents, targets and indications. Nat Rev Drug Discov *16*, 829–842. https://doi.org/10.1038/nrd.2017.178.

17. Thompson, M.D., Hendy, G.N., Percy, M.E., Bichet, D.G., and Cole, D.E.C. (2014). G protein-coupled receptor mutations and human genetic disease. Methods Mol Biol *1175*, 153–187. https://doi.org/10.1007/978-1-4939-0956-8_8.

18. Weis, W.I., and Kobilka, B.K. (2018). The Molecular Basis of G Protein-Coupled Receptor Activation. Annu Rev Biochem *87*, 897–919. https://doi.org/10.1146/annurev-biochem-060614-033910.

19. Jiang, H., Galtes, D., Wang, J., and Rockman, H.A. (2022). G protein-coupled receptor signaling: transducers and effectors. Am J Physiol Cell Physiol *323*, C731–C748. https://doi.org/10.1152/ajpcell.00210.2022.

20. Heredia, J.D., Park, J., Brubaker, R.J., Szymanski, S.K., Gill, K.S., and Procko, E. (2018). Mapping Interaction Sites on Human Chemokine Receptors by Deep Mutational Scanning. J Immunol *200*, 3825–3839. https://doi.org/10.4049/jimmunol.1800343.

21. Park, J., Selvam, B., Sanematsu, K., Shigemura, N., Shukla, D., and Procko, E. (2019). Structural architecture of a dimeric class C GPCR based on co-trafficking of sweet taste receptor subunits. J Biol Chem *294*, 4759–4774. https://doi.org/10.1074/jbc.RA118.006173.

22. Penn, W.D., McKee, A.G., Kuntz, C.P., Woods, H., Nash, V., Gruenhagen, T.C., Roushar, F.J., Chandak, M., Hemmerich, C., Rusch, D.B., et al. (2020). Probing biophysical sequence constraints within the transmembrane domains of rhodopsin by deep mutational scanning. Sci Adv *6*, eaay7505. https://doi.org/10.1126/sciadv.aay7505.

23. Jones, E.M., Lubock, N.B., Venkatakrishnan, A.J., Wang, J., Tseng, A.M., Paggi, J.M., Latorraca, N.R., Cancilla, D., Satyadi, M., Davis, J.E., et al. (2020). Structural and functional characterization of G protein-coupled receptors with deep mutational scanning. Elife *9*, e54895. https://doi.org/10.7554/eLife.54895.

24. Howard, M.K., Hoppe, N., Huang, X.-P., Mitrovic, D., Billesbølle, C.B., Macdonald, C.B., Mehrotra, E., Rockefeller Grimes, P., Trinidad, D.D., Delemotte, L., et al. (2024). Molecular basis of proton sensing by G protein-coupled receptors. Cell, S0092-8674(24)01373-4. https://doi.org/10.1016/j.cell.2024.11.036.

25. Pándy-Szekeres, G., Caroli, J., Mamyrbekov, A., Kermani, A.A., Keserű, G.M., Kooistra, A.J., and Gloriam, D.E. (2023). GPCRdb in 2023: state-specific structure models using AlphaFold2 and new ligand resources. Nucleic Acids Res *51*, D395–D402. https://doi.org/10.1093/nar/gkac1013.

26. Muppidi, J.R., Schmitz, R., Green, J.A., Xiao, W., Larsen, A.B., Braun, S.E., An, J., Xu, Y., Rosenwald, A., Ott, G., et al. (2014). Loss of signalling via Gα13 in germinal centre B-cell-derived lymphoma. Nature *516*, 254–258. https://doi.org/10.1038/nature13765.

27. Muppidi, J.R., Lu, E., and Cyster, J.G. (2015). The G protein-coupled receptor P2RY8 and follicular dendritic cells promote germinal center confinement of B cells, whereas S1PR3 can contribute to their dissemination. J Exp Med *212*, 2213–2222. https://doi.org/10.1084/jem.20151250.

28. Gallman, A.E., Wolfreys, F.D., Nguyen, D.N., Sandy, M., Xu, Y., An, J., Li, Z., Marson, A., Lu, E., and Cyster, J.G. (2021). Abcc1 and Ggt5 support lymphocyte guidance through export and catabolism of S-geranylgeranyl-l-glutathione. Sci Immunol *6*, eabg1101. https://doi.org/10.1126/sciimmunol.abg1101.

29. Lu, E., Wolfreys, F.D., Muppidi, J.R., Xu, Y., and Cyster, J.G. (2019). S-Geranylgeranyl-L-glutathione is a ligand for human B cell-confinement receptor P2RY8. Nature *567*, 244–248. https://doi.org/10.1038/s41586-019-1003-z.

30. Lu, E., and Cyster, J.G. (2019). G-protein coupled receptors and ligands that organize humoral immune responses. Immunol Rev *289*, 158–172. https://doi.org/10.1111/imr.12743.

31. Lohr, J.G., Stojanov, P., Lawrence, M.S., Auclair, D., Chapuy, B., Sougnez, C., Cruz-Gordillo, P., Knoechel, B., Asmann, Y.W., Slager, S.L., et al. (2012). Discovery and prioritization of somatic mutations in diffuse large B-cell lymphoma (DLBCL) by whole-exome sequencing. Proc Natl Acad Sci U S A *109*, 3879–3884. https://doi.org/10.1073/pnas.1121343109.

32. Sondka, Z., Dhir, N.B., Carvalho-Silva, D., Jupe, S., Madhumita, null, McLaren, K., Starkey, M., Ward, S., Wilding, J., Ahmed, M., et al. (2024). COSMIC: a curated database of somatic variants and clinical data for cancer. Nucleic Acids Res *52*, D1210–D1217. https://doi.org/10.1093/nar/gkad986.

33. He, Y., Gallman, A.E., Xie, C., Shen, Q., Ma, J., Wolfreys, F.D., Sandy, M., Arsov, T., Wu, X., Qin, Y., et al. (2022). P2RY8 variants in lupus patients uncover a role for the receptor in immunological tolerance. J Exp Med *219*, e20211004. https://doi.org/10.1084/jem.20211004.

34. Olvera-León, R., Zhang, F., Offord, V., Zhao, Y., Tan, H.K., Gupta, P., Pal, T., Robles-Espinoza, C.D., Arriaga-González, F.G., Matsuyama, L.S.A.S., et al. (2024). High-resolution functional mapping of RAD51C by saturation genome editing. Cell *187*, 5719-5734.e19. https://doi.org/10.1016/j.cell.2024.08.039.

35. Hsu, C., Nisonoff, H., Fannjiang, C., and Listgarten, J. (2022). Learning protein fitness models from evolutionary and assay-labeled data. Nat Biotechnol *40*, 1114–1122. https://doi.org/10.1038/s41587-021-01146-5.

36. Isberg, V., de Graaf, C., Bortolato, A., Cherezov, V., Katrich, V., Marshall, F.H., Mordalski, S., Pin, J.-P., Stevens, R.C., Vriend, G., et al. (2015). Generic GPCR residue numbers -

1271   aligning topology maps while minding the gaps. Trends Pharmacol Sci *36*, 22–31.
1272   https://doi.org/10.1016/j.tips.2014.11.001.

1273   37. Gacasan, S.B., Baker, D.L., and Parrill, A.L. (2017). G protein-coupled receptors: the
1274   evolution of structural insight. AIMS Biophys *4*, 491–527.
1275   https://doi.org/10.3934/biophy.2017.3.491.

1276   38. Ballesteros, J.A., and Weinstein, H. (1995). [19] Integrated methods for the construction of
1277   three-dimensional models and computational probing of structure-function relations in G
1278   protein-coupled receptors. In Methods in Neurosciences Receptor Molecular Biology., S. C.
1279   Sealfon, ed. (Academic Press), pp. 366–428. https://doi.org/10.1016/S1043-9471(05)80049-
1280   7.

1281   39. Barros-Álvarez, X., Nwokonko, R.M., Vizurraga, A., Matzov, D., He, F., Papasergi-Scott,
1282   M.M., Robertson, M.J., Panova, O., Yardeni, E.H., Seven, A.B., et al. (2022). The tethered
1283   peptide activation mechanism of adhesion GPCRs. Nature *604*, 757.
1284   https://doi.org/10.1038/s41586-022-04575-7.

1285   40. Nehmé, R., Carpenter, B., Singhal, A., Strege, A., Edwards, P.C., White, C.F., Du, H.,
1286   Grisshammer, R., and Tate, C.G. (2017). Mini-G proteins: Novel tools for studying GPCRs
1287   in their active conformation. PLoS One *12*, e0175642.
1288   https://doi.org/10.1371/journal.pone.0175642.

1289   41. Lu, M., and Wu, B. (2016). Structural studies of G protein-coupled receptors. IUBMB Life
1290   *68*, 894–903. https://doi.org/10.1002/iub.1578.

1291   42. Olsen, R.H.J., DiBerto, J.F., English, J.G., Glaudin, A.M., Krumm, B.E., Slocum, S.T., Che,
1292   T., Gavin, A.C., McCorvy, J.D., Roth, B.L., et al. (2020). TRUPATH, an open-source
1293   biosensor platform for interrogating the GPCR transducerome. Nat Chem Biol *16*, 841–849.
1294   https://doi.org/10.1038/s41589-020-0535-8.

1295   43. DiBerto, J.F., Olsen, R.H.J., and Roth, B.L. (2022). TRUPATH: An Open-Source Biosensor
1296   Platform for Interrogating the GPCR Transducerome. Methods Mol Biol *2525*, 185–195.
1297   https://doi.org/10.1007/978-1-0716-2473-9_13.

1298   44. Dixon, A.S., Schwinn, M.K., Hall, M.P., Zimmerman, K., Otto, P., Lubben, T.H., Butler,
1299   B.L., Binkowski, B.F., Machleidt, T., Kirkland, T.A., et al. (2016). NanoLuc
1300   Complementation Reporter Optimized for Accurate Measurement of Protein Interactions in
1301   Cells. ACS Chem Biol *11*, 400–408. https://doi.org/10.1021/acschembio.5b00753.

1302   45. Tate, J.G., Bamford, S., Jubb, H.C., Sondka, Z., Beare, D.M., Bindal, N., Boutselakis, H.,
1303   Cole, C.G., Creatore, C., Dawson, E., et al. (2019). COSMIC: the Catalogue Of Somatic
1304   Mutations In Cancer. Nucleic Acids Res *47*, D941–D947.
1305   https://doi.org/10.1093/nar/gky1015.

1306   46. Ursu, O., Neal, J.T., Shea, E., Thakore, P.I., Jerby-Arnon, L., Nguyen, L., Dionne, D., Diaz,
1307   C., Bauman, J., Mosaad, M.M., et al. (2022). Massively parallel phenotyping of coding

1308   variants in cancer with Perturb-seq. Nat Biotechnol *40*, 896–905.
1309   https://doi.org/10.1038/s41587-021-01160-7.

1310 47. Andrews, S. (2010). FastQC: A Quality Control Tool for High Throughput Sequence Data.
1311   Available online.

1312 48. Bushnell, B. BBTools software package. Available online.

1313 49. Bushnell, B., Rood, J., and Singer, E. (2017). BBMerge - Accurate paired shotgun read
1314   merging via overlap. PLoS One *12*, e0185056. https://doi.org/10.1371/journal.pone.0185056.

1315 50. McKenna, A., Hanna, M., Banks, E., Sivachenko, A., Cibulskis, K., Kernytsky, A.,
1316   Garimella, K., Altshuler, D., Gabriel, S., Daly, M., et al. (2010). The Genome Analysis
1317   Toolkit: a MapReduce framework for analyzing next-generation DNA sequencing data.
1318   Genome Res *20*, 1297–1303. https://doi.org/10.1101/gr.107524.110.

1319 51. Van der Auwera, G.A., and O'Connor, B.D. (2020). Genomics in the Cloud: Using Docker,
1320   GATK, and WDL in Terra (O'Reilly Media).

1321 52. Rubin, A.F., Gelman, H., Lucas, N., Bajjalieh, S.M., Papenfuss, A.T., Speed, T.P., and
1322   Fowler, D.M. (2017). A statistical framework for analyzing deep mutational scanning data.
1323   Genome Biol *18*, 150. https://doi.org/10.1186/s13059-017-1272-5.

1324 53. Rives, A., Meier, J., Sercu, T., Goyal, S., Lin, Z., Liu, J., Guo, D., Ott, M., Zitnick, C.L., Ma,
1325   J., et al. (2021). Biological structure and function emerge from scaling unsupervised learning
1326   to 250 million protein sequences. Proc Natl Acad Sci U S A *118*, e2016239118.
1327   https://doi.org/10.1073/pnas.2016239118.

1328 54. Barsi-Rhyne, B., Manglik, A., and von Zastrow, M. (2022). Discrete GPCR-triggered
1329   endocytic modes enable β-arrestins to flexibly regulate cell signaling. Elife *11*, e81563.
1330   https://doi.org/10.7554/eLife.81563.

1331 55. Schindelin, J., Arganda-Carreras, I., Frise, E., Kaynig, V., Longair, M., Pietzsch, T.,
1332   Preibisch, Rueden, C., Saalfeld, S., Schmid, B., et al. (2012). Fiji: an open-source platform
1333   for biological-image analysis. Nature methods *9*. https://doi.org/10.1038/nmeth.2019.

1334 56. Staus, D.P., Wingler, L.M., Choi, M., Pani, B., Manglik, A., Kruse, A.C., and Lefkowitz, R.J.
1335   (2018). Sortase ligation enables homogeneous GPCR phosphorylation to reveal diversity in
1336   β-arrestin coupling. Proc Natl Acad Sci U S A *115*, 3834–3839.
1337   https://doi.org/10.1073/pnas.1722336115.

1338 57. Billesbølle, C.B., de March, C.A., van der Velden, W.J.C., Ma, N., Tewari, J., Del Torrent,
1339   C.L., Li, L., Faust, B., Vaidehi, N., Matsunami, H., et al. (2023). Structural basis of odorant
1340   recognition by a human odorant receptor. Nature *615*, 742–749.
1341   https://doi.org/10.1038/s41586-023-05798-y.

58. Chen, H., Chen, K., Huang, W., Staudt, L.M., Cyster, J.G., and Li, X. (2022). Structure of S1PR2-heterotrimeric G13 signaling complex. Sci Adv *8*, eabn0067. https://doi.org/10.1126/sciadv.abn0067.

59. Croll, T.I. (2018). ISOLDE: a physically realistic environment for model building into low-resolution electron-density maps. Acta Crystallogr D Struct Biol *74*, 519–530. https://doi.org/10.1107/S2059798318002425.

60. Adams, P.D., Afonine, P.V., Bunkóczi, G., Chen, V.B., Davis, I.W., Echols, N., Headd, J.J., Hung, L.-W., Kapral, G.J., Grosse-Kunstleve, R.W., et al. (2010). PHENIX: a comprehensive Python-based system for macromolecular structure solution. Acta Crystallogr D Biol Crystallogr *66*, 213–221. https://doi.org/10.1107/S0907444909052925.

61. Emsley, P., and Cowtan, K. (2004). Coot: model-building tools for molecular graphics. Acta Crystallogr D Biol Crystallogr *60*, 2126–2132. https://doi.org/10.1107/S0907444904019158.

62. Moriarty, N.W., Grosse-Kunstleve, R.W., and Adams, P.D. (2009). electronic Ligand Builder and Optimization Workbench (eLBOW): a tool for ligand coordinate and restraint generation. Acta Crystallogr D Biol Crystallogr *65*, 1074–1080. https://doi.org/10.1107/S0907444909029436.

63. Barad, B.A., Echols, N., Wang, R.Y.-R., Cheng, Y., DiMaio, F., Adams, P.D., and Fraser, J.S. (2015). EMRinger: side chain-directed model and map validation for 3D cryo-electron microscopy. Nat Methods *12*, 943–946. https://doi.org/10.1038/nmeth.3541.

64. Goddard, T.D., Huang, C.C., Meng, E.C., Pettersen, E.F., Couch, G.S., Morris, J.H., and Ferrin, T.E. (2018). UCSF ChimeraX: Meeting modern challenges in visualization and analysis. Protein science : a publication of the Protein Society *27*. https://doi.org/10.1002/pro.3235.

65. Meng, E.C., Goddard, T.D., Pettersen, E.F., Couch, G.S., Pearson, Z.J., Morris, J.H., and Ferrin, T.E. (2023). UCSF ChimeraX: Tools for structure building and analysis. Protein Sci *32*, e4792. https://doi.org/10.1002/pro.4792.

66. Cyster, J.G., Shotton, D.M., and Williams, A.F. (1991). The dimensions of the T lymphocyte glycoprotein leukosialin and identification of linear protein epitopes that can be modified by glycosylation. EMBO J *10*, 893–902. https://doi.org/10.1002/j.1460-2075.1991.tb08022.x.
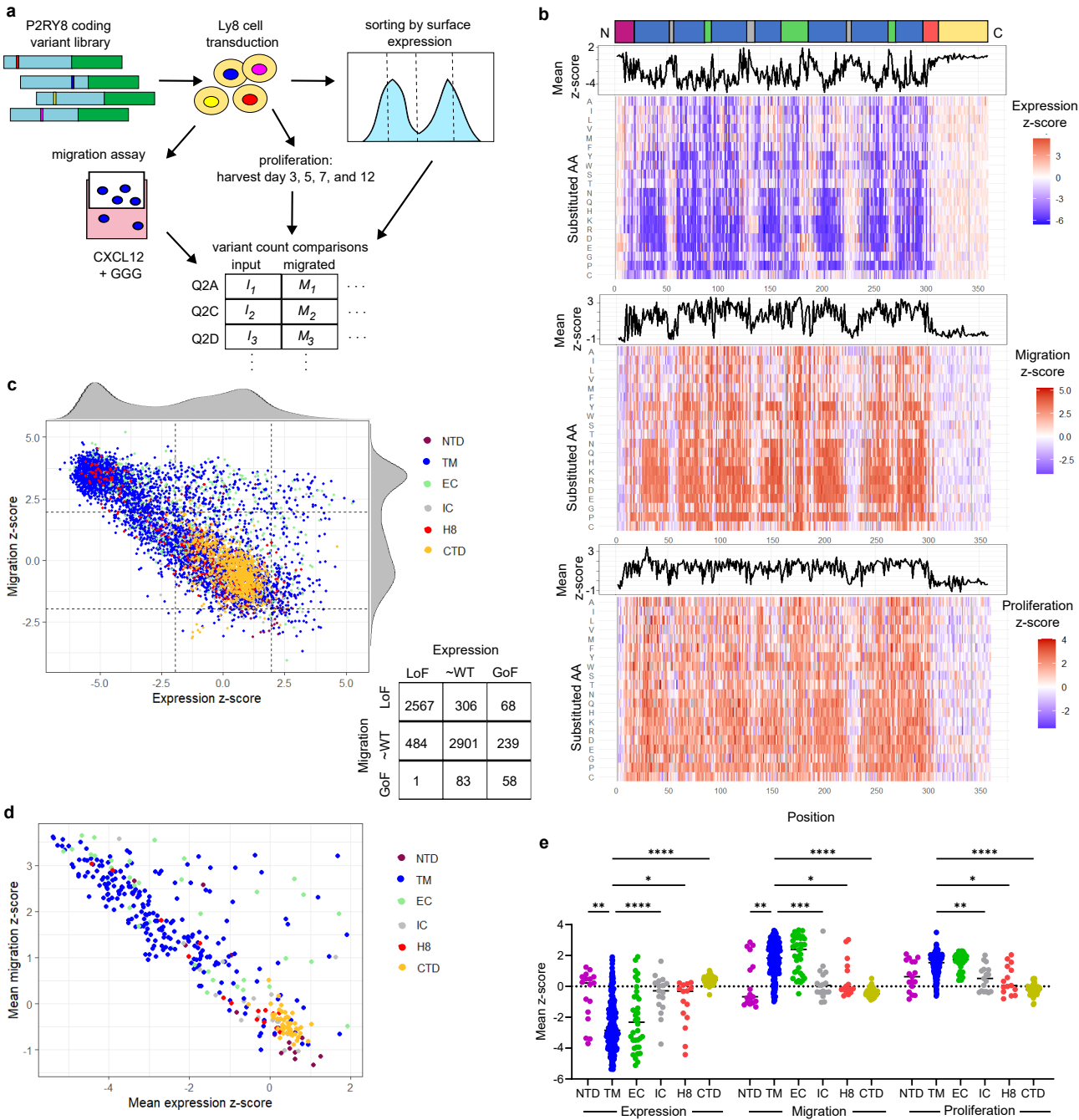
Figures:

Figure 1

Fig. 1: DMS of P2RY8 across three phenotypes. a, Schematic of DMS approach **b,** Heat maps of surface expression, migration, and proliferation z-scores with line plots of mean z-score for each position, **c,** Plot comparing expression and migration z-scores of missense variants, colored by protein domain, with table showing variant count by section, boundaries at z-scores of 2 and -2. **d,** Plot comparing expression and migration mean z-scores for each position, colored by protein domain. **e,** Expression, migration, and proliferation mean z-scores for each position, partitioned by protein domain; lines are medians. Negative z-scores are LoF for expression, GoF for migration or proliferation. Welch ANOVA test with Dunnett's T3 multiple comparisons test; for each assay TM compared to the five other domains; adjusted p-value * < 0.05, ** <0.01, *** < 0.001, **** < 0.0001. C, C-terminus; CTD, C-terminal domain; EC, extracellular loop; GoF, gain-of-function; H8, helix 8; IC, intracellular loop; LoF, loss-of-function; N, N-terminus; NTD, N-terminal domain; TM, transmembrane domain.
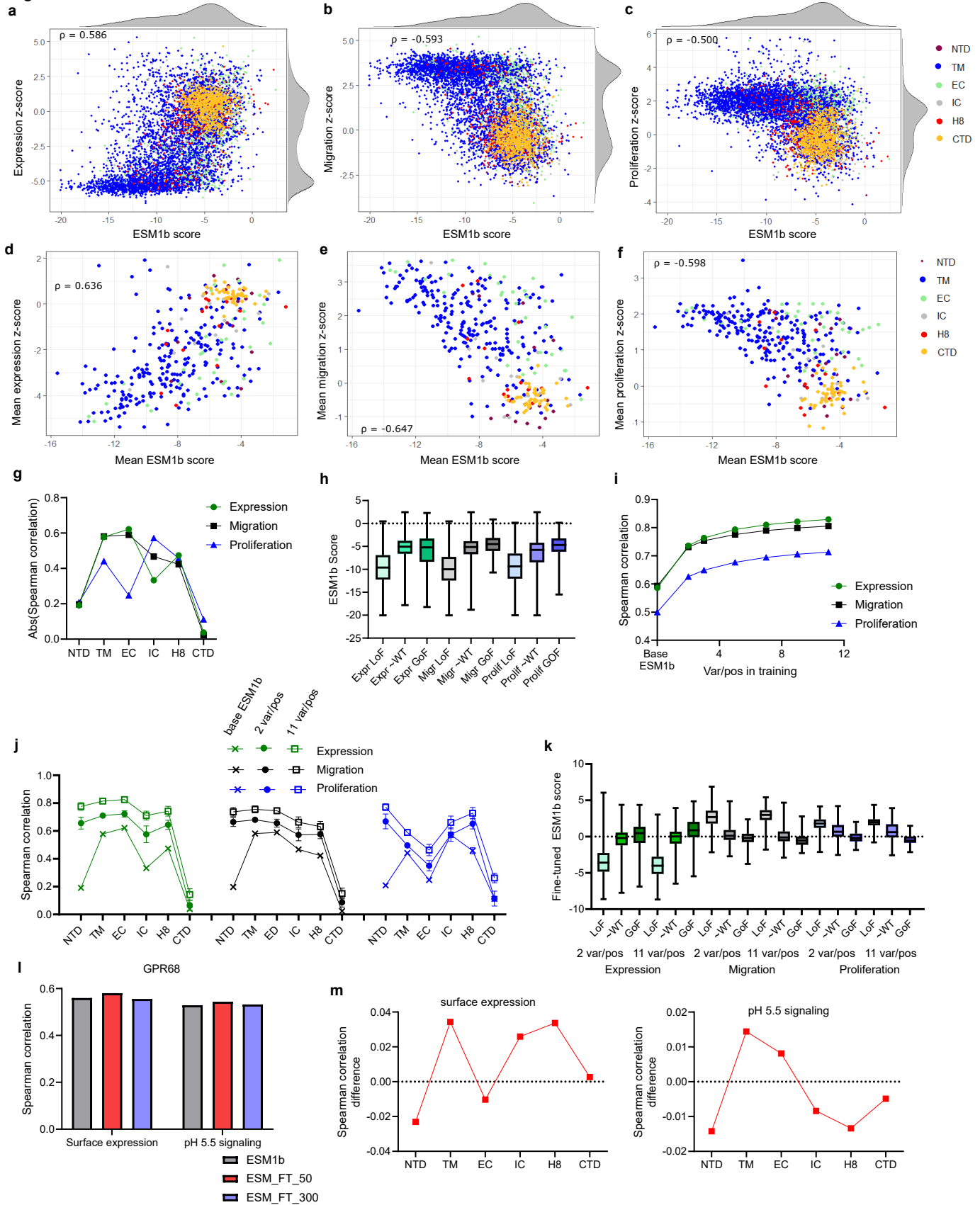
Figure 2

Fig. 2: Improving computational variant effect prediction using limited experimental data.
a-c Plots comparing ESM1b scores and **(a)** expression z-score, **(b)** migration z-score, or **(c)** proliferation z-score for each variant, colored by protein domain. **d-f** Plots comparing mean ESM1b score and **(d)** expression mean z-score, **(e)** migration mean z-score, or **(f)** proliferation mean z-score for each position, colored by protein domain. **g,** Plot of Spearman correlation between ESM1b score and variant expression, migration, and proliferation z-scores, partitioned by protein domain. **h,** Plot comparing distribution of ESM1b scores for each variant, partitioned by DMS phenotype. Whiskers extend to maximum and minimum, boxes shows 25th percentile, median, and 75th percentile. **i,** Plot of Spearman correlation between fine-tuned ESM1b scores and DMS z-scores as training set size varies. Shows mean and SD (k = 50). **j,** Plot comparing Spearman correlation when using ESM1b score or fine-tuned ESM1b scores with 2 variants/position or 11 variants/position training sets, partitioned by domain. Shows means and SD (k = 50). **k,** Plot comparing distribution of fine-tuned ESM1b scores for representative 2 variant per position training and representative 11 variant per position training, partitioned by DMS phenotype. Whiskers extend to maximum and minimum, boxes shows 25th percentile, median, and 75th percentile. **l,** Plot comparing Spearman correlations between human GPR68 DMS results[24] and base ESM1b or ESM1b fine-tuned on P2RY8 expression results for 50 or 300 fine-tuning steps. **m,** Plots showing difference in Spearman correlation between base ESM1b and 50-step fine-tuned ESM1b on GPR68 surface expression (L) or pH 5.5 signaling (R) (value > 0 indicates greater correlation with fine-tuning). In **g, i, j,** sign inverted for migration and proliferation so all three correlations have same sign. CTD, C-terminal domain; EC, extracellular loop; GoF, gain-of-function, z-score > 2 for expression, < -2 for migration, proliferation; H8, helix 8; IC, intracellular loop; LoF, loss-of-function, z-score < -2 for expression, > 2 for migration, proliferation; NTD, N-terminal domain; TM, transmembrane helices; ρ, Spearman correlation coefficient.
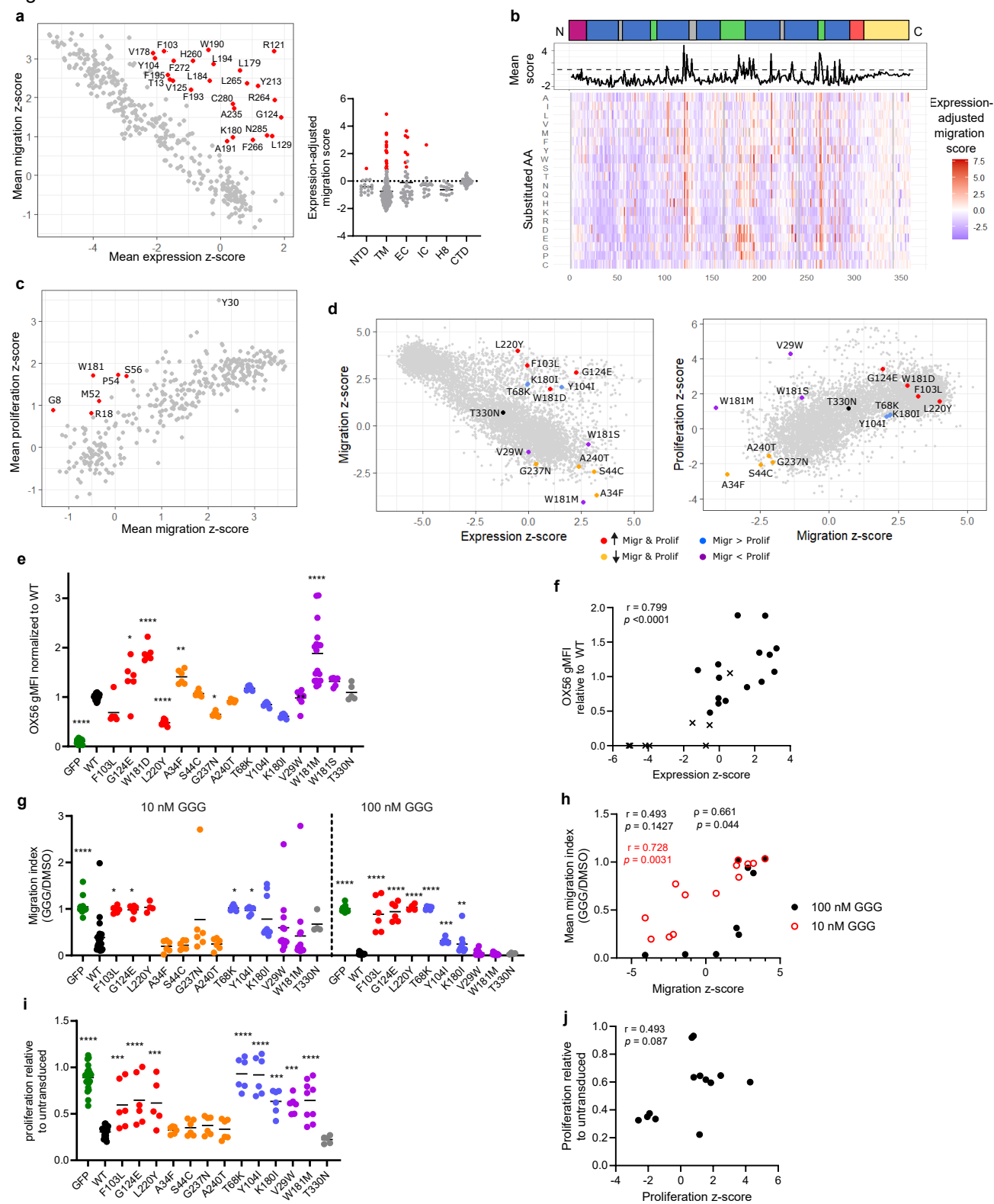
Figure 3

Fig. 3: Validation of variants with independent effects on expression and function. a, (L) Plot comparing expression and migration mean z-scores for each position, those with high expression-adjusted migration scores are colored red; (R) Expression-adjusted migration score for each position, partitioned by domain, lines are medians. **b,** Heat map of expression-adjusted migration score for each variant, as well as line plot of mean expression-adjusted migration scores by position. **c,** Plot comparing migration and proliferation mean z-scores for each position, those with high migration-adjusted proliferation score are colored red. **d,** Plots comparing expression and migration z-scores (L) or migration and proliferation z-scores (R), with select variants labeled. **e,** P2RY8 surface expression normalized to WT P2RY8, lines are means. Pooled results from 9 experiments, total 5 to 26 biological replicates per condition. **f,** Plot of DMS expression z-score and WT-normalized expression for select variants, circles are variants in **d**, crosses are variants assayed previously[26,29]. **g,** Migration of cells toward CXCL12 in the presence of GGG, relative to DMSO (vehicle); each dot is a biological replicate, lines are means. Pooled results from 9 experiments, total 4 to 23 biological replicates per condition. **h,** Plot of DMS migration z-score and migration indices for variants shown in **g. i,** Proliferation over 13 days relative to untransduced cells in same well; each point is a biological replicate, lines are means. Pooled results from 8 experiments, total 5 to 21 biological replicates per condition. **j,** Plot of DMS proliferation z-score and proliferation relative to untransduced cells for variants shown in **i. e, g, i,** One-way ANOVA test with Dunnett's multiple comparisons test, each variant compared to WT; adjusted p-value * < 0.05, ** <0.01, *** <0.001, **** < 0.0001. **f, h, j,** Two-tailed p-values; r, Pearson correleation coefficient; ρ, Spearman correlation coefficient.
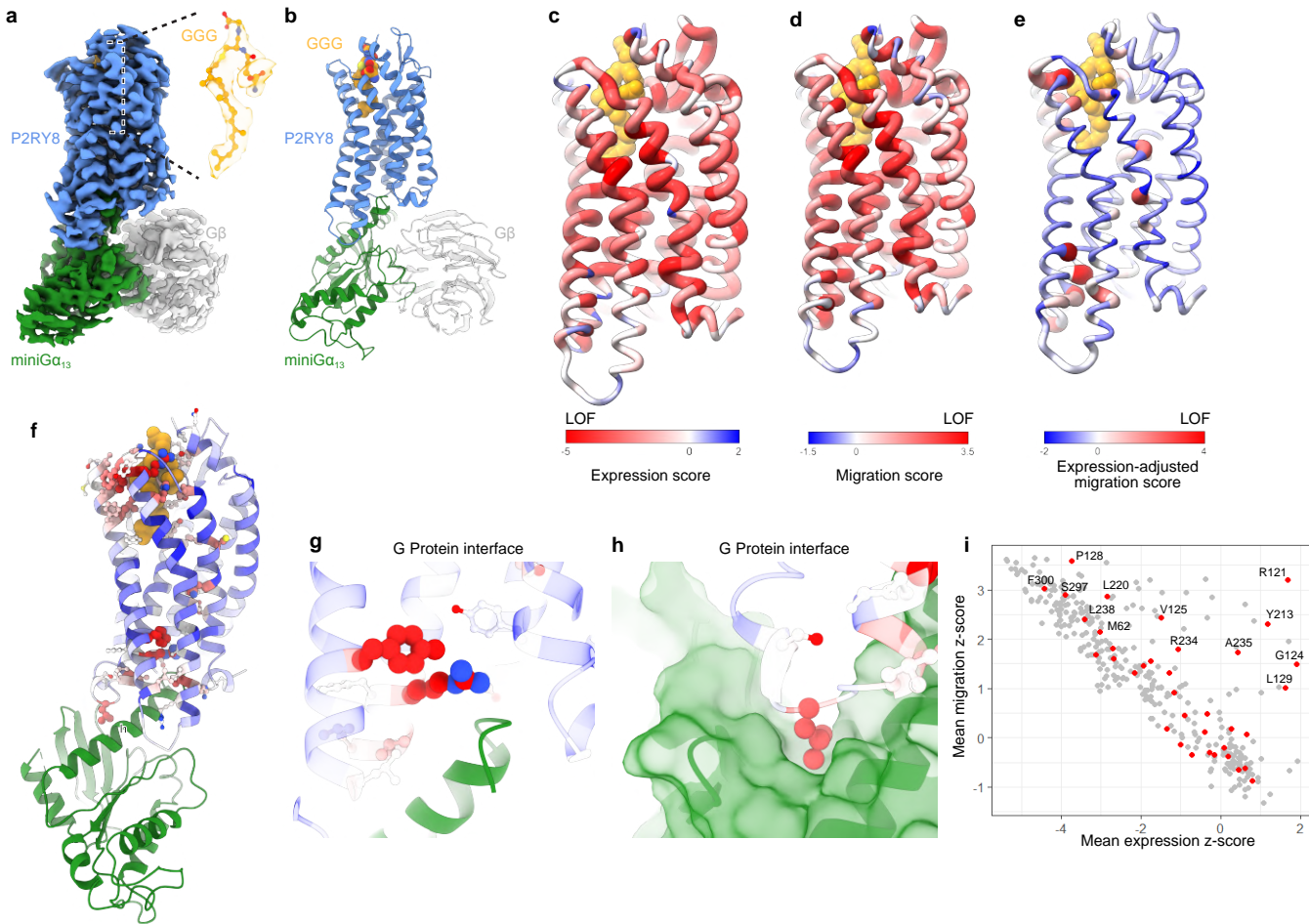
1481 **Fig. 4: Structure of activated ligand-bound human P2RY8. a,b,** Cryo-EM density map **(a)**
1482 and ribbon model **(b)** of active human P2RY8 bound to GGG (orange). P2RY8 is fused to mini-
1483 Gα_{13} (green) and bound to Gβ_1 (grey). **c, d,e,** Ribbon model of P2RY8 colored to indicate DMS
1484 mean effect sizes for expression **(c)**, migration **(d)**, and expression-adjusted migration score **(e)**.
1485 Grey indicates positions with no data available. **f, g, h,** Expression-adjusted migration scores for
1486 individual residues with close-up views of **(g)** D(E)-R-Y motif and **(h)** G-protein interface. **i,** Plot
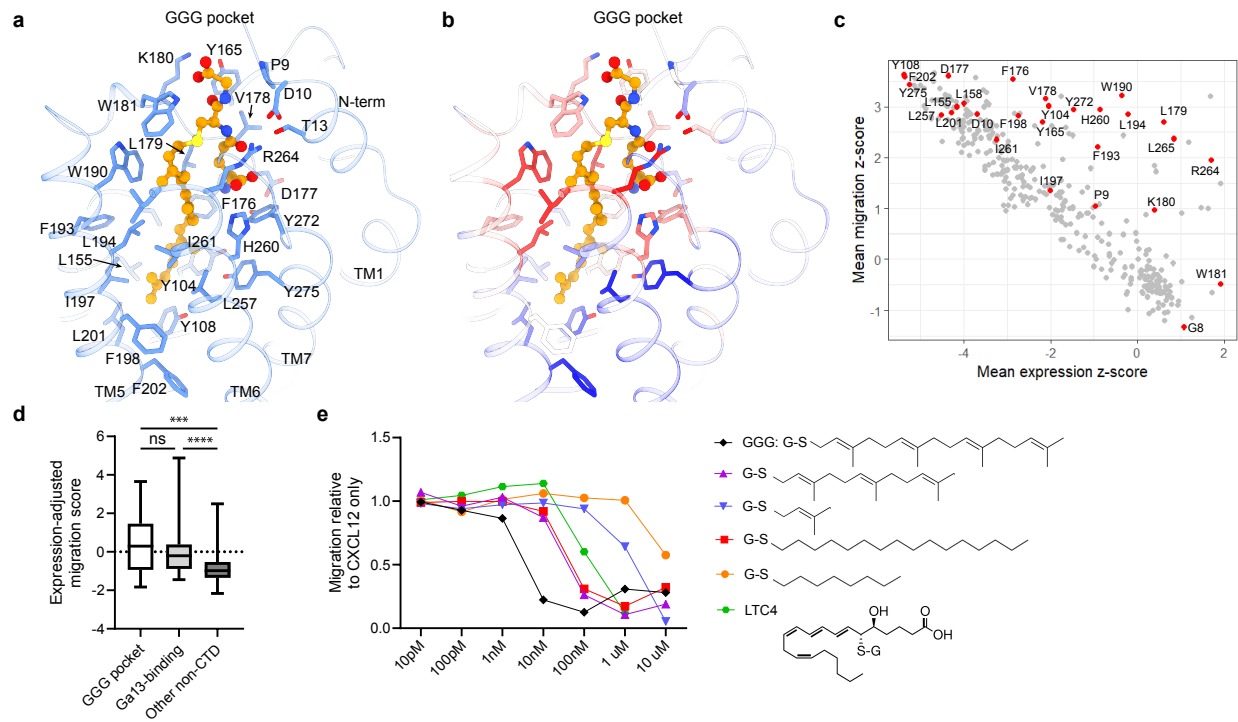1487 comparing expression and migration mean z-scores by position, with Gα_{13}-interacting positions
1488 colored red.

1489

1490

1491

1492

1493

1494

1495

1496

1497

1498

1499

1500

1501

1502

1503

1504

1505

1506

1507

1508

1509

1510

a GGG pocket

b GGG pocket

c

d

e

Panel e legend:
- GGG: G-S
- G-S
- G-S
- G-S
- G-S
- LTC4

x-axis (panel e): 10pM 100pM 1nM 10nM 100nM 1 UM 10 UM

y-axis (panel e): Migration relative to CXCL12 only

Panel c axes:
- x-axis: Mean expression z-score
- y-axis: Mean migration z-score

Panel d axes:
- y-axis: Expression-adjusted migration score
- x-axis categories: GGG pocket, Gα13-binding, Other non-CTD
- significance: ns, ***, ****

Fig. 5: Structural features of GGG recognition. a,b, Close-up view of the GGG binding site in P2RY8. **A,** Expression effect sizes mapped onto P2RY8 residues (sticks and ribbon) that form the GGG binding site (orange sticks and spheres). **b,** Migration effect sizes mapped onto P2RY8 residues (sticks and ribbon) that form the GGG binding site (orange sticks and spheres). **c,** Plot comparing expression and migration mean z-scores by position, with GGG-interacting positions colored red. **d,** Distribution of expression-adjusted migration scores for GGG-binding pocket residues, $G\alpha_{13}$-contacting residues, and other non-CTD residues. Whiskers extend to maximum and minimum, boxes shows 25th percentile, median, and 75th percentile**.** Kruskal-Wallis test with Dunn's multiple comparisons test, ns = nonsignificant, *** < 0.001, **** < 0.0001. **e,** Assay of inhibition of P2RY8-transduced WEHI-231 cells, in the presence of 50 ng mL^{-1} CXCL12 with or without GGG or candidate P2RY8 ligands of varying concentrations, normalized to migration to CXCL12 alone. Representative results from one of two independent experiments. G-S, glutathione; LTC4, leukotriene C$_4$.
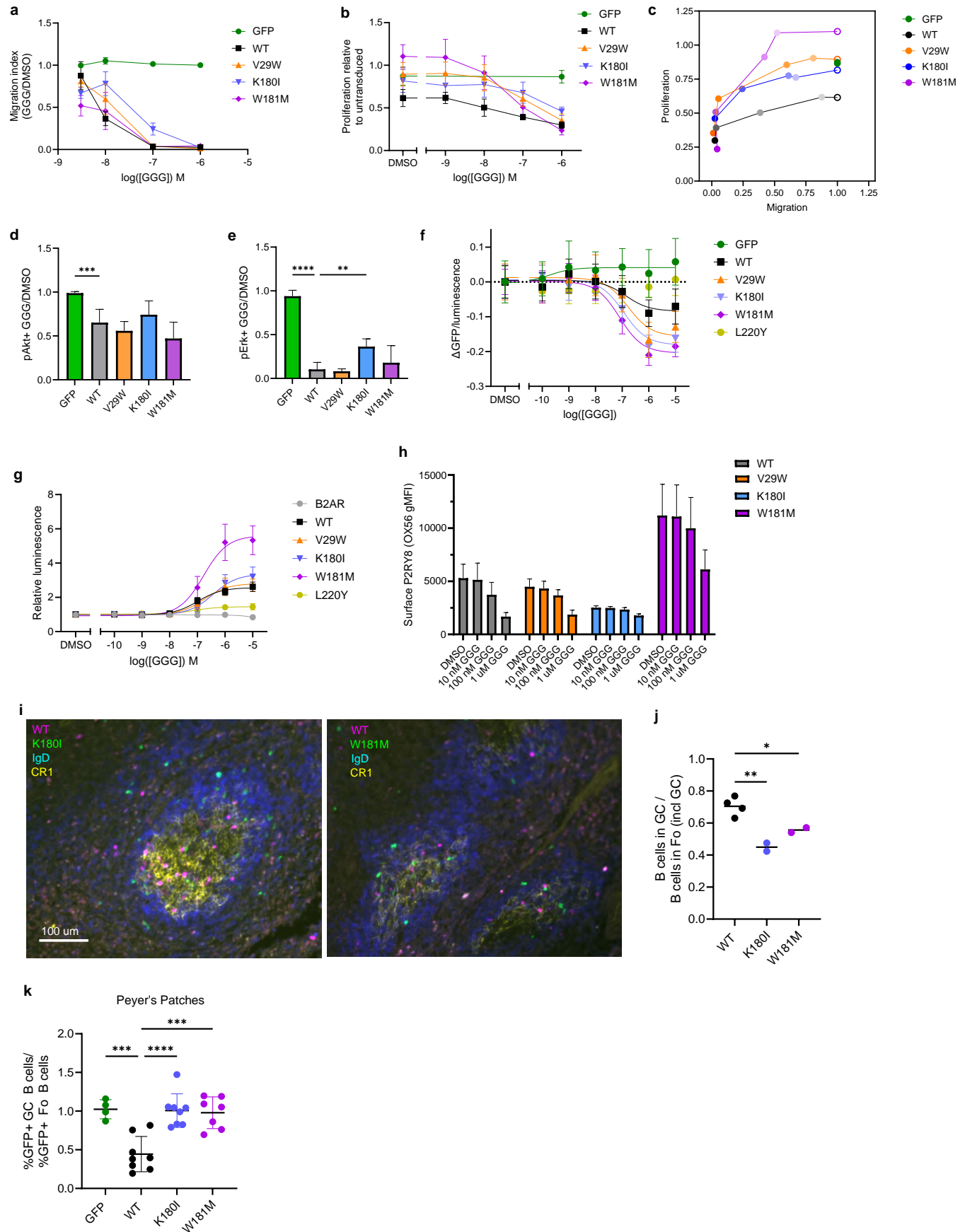
Figure 6

Fig. 6: In vitro and in vivo delineation of heterogeneous variants effects. a, Migration of transduced Ly8 cells toward CXCL12 with varying concentrations of GGG, relative to DMSO (vehicle), and normalized to untransduced cells; points are means, error bars are SDs. Pooled results from 10 experiments, total 2 to 22 (mean 9.5, SD 4.9) replicates per condition. **b,** Proliferation over 7 days relative to untransduced cells in same well, with varying concentrations of exogenous GGG; points are means, error bars are SDs Pooled results from 5 experiments, total 6 to 12 replicates per condition. **c,** Migration and proliferation phenotypes at different GGG doses (comparing data from **a** and **b**). Empty circle indicates DMSO (vehicle), and ascendingly dark shading indicates 1 nM proliferation/3 nM migration, 10 nM, 100 nM, and 1 μM. **d,e** Transduced Ly8 cells exposed to GGG or vehicle were assayed using phospho-flow cytometry; graphs show ratio of pAkt$^+$ (**d**) or pErk$^+$ (**e**) cells in GGG vs vehicle, normalized to GFP (empty vector). Bars are means, error bars are SDs. Pooled results from 4 experiments, total 6 replicates per condition. **f,** BRET assay: 293T cells, co-transfected with P2RY8 variant, RLuc-Gα$_{13}$ fusion, Gβ, and Gγ-GFP fusion, were treated with varying GGG concentrations and ratio of luminescence and GFP fluorescence determined, ratio normalized to DMSO (vehicle) condition. Points are means, error bars are SDs. Curves fit using log(inhibitor) vs response, 3 parameter model (Prism, Graphpad). Pooled results from 4 experiments, total 9 to 12 replicates per condition. **g,** NanoBiT assay: 293T cells co-transfected with GPCR-LgBiT and β-arrestin-SmBiT, treated with varying concentrations of GGG. Luminescence relative to DMSO (vehicle) plotted. Points are means, error bars are SDs. Curves fit using log(agonist) vs response, 3 parameter mode (Prism, Graphpad). Pooled results from 4 experiments, total 12 replicates per condition. **h,** P2RY8 surface expression of transduced Ly8 cells after 45 minute treatment with varying concentrations of GGG. Pooled from 3 experiments, total 6 to 8 replicates per condition. **i,** Representative immunofluorescence micrographs; activated polyclonal B cells transduced with K180I-GFP or W181M-GFP were co-transferred (~3:2 ratio) with WT-TagBFP into SRBC immunized recipient mice; anti-GFP (green), anti-TagBFP (magenta), anti-CR1 (yellow, GC label), and IgD (blue, follicular B cell label); scale bar 100 μm, both images same scale. **j,** Quantitation of co-transferred transduced cells: ratio of transduced (GFP$^+$ or BFP$^+$) cells within the GC to those within the follicle (including GC), each dot is one mouse (a given mouse is represented by one WT dot and one K180I or W181M dot). Two independent experiments, one recipient mouse per variant per experiment, at least 45 GCs analyzed per mouse. **k,** Irradiated CD45.1 mice were reconstituted with bone marrow transduced with EV-GFP, WT-P2RY8-GFP, K180I-GFP, or W181M-GFP. After reconstitution, Peyer's patches were analyzed for the frequency of GFP+ cells among GC and follicular B cells and the ratio plotted. Each point is a mouse. Mean and SD shown. Pooled from 3 experiments, total 4 to 8 mice per condition. **d, e, j, k,** One-way ANOVA test with Dunnett's multiple comparisons test, each variant compared to WT; adjusted p-value ** < 0.01, *** <0.001, **** < 0.0001.
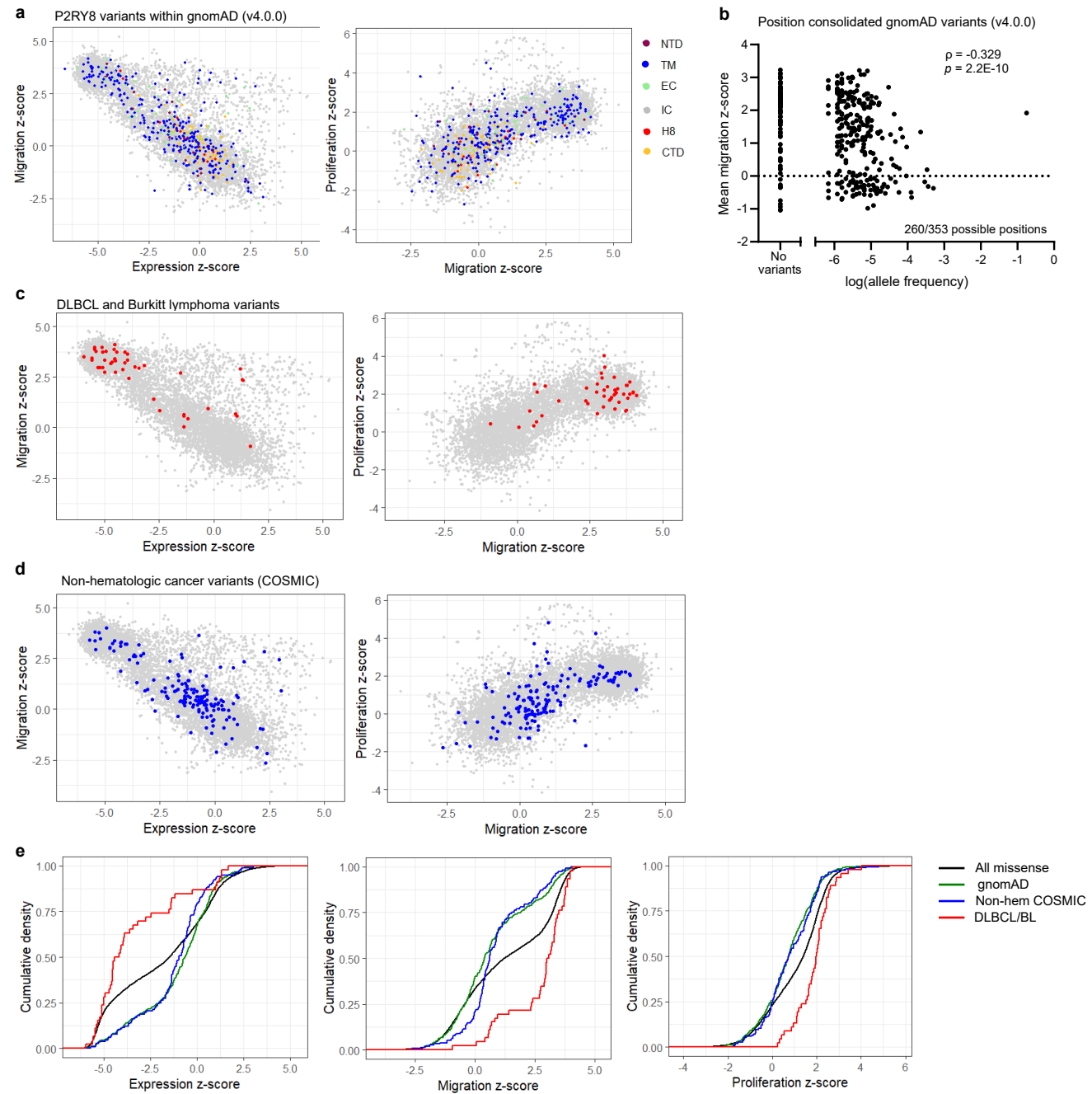
Figure 7

Fig. 7: Phenotypes of germline and lymphoma-associated P2RY8 variants. a, Plots comparing expression and migration z-scores (L) and migration and proliferation z-scores (R) of variants, with human population data in gnomAD (v4.0.0) colored by domain of protein. **b,** Plot of allele frequency for missense variants in gnomAD (v4.0.0), summed within each position, to the mean migration z-score for each position. ρ, Spearman correlation; p-value calculated using algorithm AS 89 with Edgeworth series approximation. **c,** Plots comparing expression and migration z-scores (L) and migration and proliferation z-scores (R) of missense variants, with 48 variants reported in DLBCL or Burkitt lymphoma colored red. **d,** Plots comparing expression and migration z-scores (L) and migration and proliferation z-scores (R) of missense variants, with non-hematologic cancer variants colored blue **e,** Cumulative density plots of expression, migration, and proliferation z-scores for all missense variants (black), gnomAD (v4.0.0) variants (green), non-hematologic cancer variants (blue), and DLBCL / Burkitt lymphoma variants (red).